



Asymptotic homogenization-based strain gradient elastodynamics: Governing equations, well-posedness and numerical examples

Quanzhang Li ^{a,b}, Yipeng Rao ^c, Zihao Yang ^d, Junzhi Cui ^b, Meizhen Xiang ^a, ^{*}

^a National Key Laboratory of Computational Physics, Institute of Applied Physics and Computational Mathematics, Beijing, 100088, China

^b LSEC, ICMSEC, Academy of Mathematics and Systems Sciences, CAS, Beijing, 100090, China

^c PKU-Changsha Institute for Computing and Digital Economy, Changsha, Hunan 410205, PR China

^d School of Mathematics and Statistics, Northwestern Polytechnical University, Xian, 710072, China

ARTICLE INFO

Keywords:

Strain gradient elastodynamics
Asymptotic homogenization
Heterogeneous materials
Well-posedness

ABSTRACT

We develop a strain gradient elastodynamics model for heterogeneous materials based on the two-scale asymptotic homogenization theory. Utilizing only the first-order cell functions, the present model is more concise and more computationally efficient than previous works with high-order truncations. Furthermore, we rigorously prove that the coefficient tensors, including the homogenized elasticity tensor, the strain gradient stiffness tensor, and the micro-inertial tensor are symmetric positive definite, thereby establishing the well-posedness of the strain gradient elastodynamics model, i.e., the existence and uniqueness of solutions. Numerical simulations are performed to confirm the theoretical findings and illustrate the characteristics of the present model in comparison with classical elastodynamics model (without strain gradient terms) and strain gradient models with higher-order truncations. The results indicate that the strain gradient model derived based on the first-order truncation can achieve an optimal balance between accuracy and computational cost.

1. Introduction

Classical continuum mechanics has long been the cornerstone for analyzing mechanical behavior of materials. However, its point-to-point local stress-strain relationship fails to account for size-dependent phenomena arising from microscale nonlocal interactions [1–4]. This limitation becomes particularly evident when the largest microstructural length scales are comparable to macroscopic dimensions, as observed in porous and textile composite structures [5,6], trabecular bone [7,8], and micro-devices [9–11]. Furthermore, the classical framework leads to unphysical stress singularities at non-convex corners, such as crack tips, causing unexpected mesh-size-dependent results in numerical analyses [12,13].

To overcome these limitations, various generalized nonlocal continuum mechanics models have been proposed. For instance, Eringen extended the classical stress-strain relationship by defining the stress at a point as a volume integral of strain over a finite region [14–16]. Similarly, peridynamics reformulates continuum mechanics through integral equations that describe nonlocal interactions over finite distances, enabling a natural treatment of discontinuities such as cracks [17–19].

In addition to strong nonlocal models based on integral equations, the strain gradient model represents an alternative class of frameworks that has been extensively developed and validated for capturing nonlocal effects related to microstructures. The origins of strain gradient theory can be traced back to the pioneering work of the Cosserat brothers [20], who proposed that material points possess rotational degrees of freedom in addition to standard displacement degrees of freedom. This led to the introduction of

* Corresponding author.

E-mail address: xiang_meizhen@iapcm.ac.cn (M. Xiang).

moment stresses that supplement classical stresses. Mindlin et al. [21], Mindlin [22] and Toupin [23] later formulated comprehensive three-dimensional strain gradient theories for linear elastic materials. Since then, strain gradient models have become a prominent topic in the solid mechanics community, achieving notable success across diverse fields, including linear elasticity [3,24,25], anisotropic and dispersive wave propagation [26,27], thermoelasticity [28–30], plasticity [31–33], and fracture mechanics [34–37].

A major challenge that limits application of the early-developed strain gradient models is to determine the material parameters associated with the high-order terms. These parameters are generally difficult to be measured experimentally. Over the past decades, continuous efforts have been directed toward determining the higher-order gradient modulus through ‘bottom-up’ multiscale techniques, linking strain gradient models to microstructural features. Several studies (e.g., [38–40]) have focused on deriving higher-order elasticity tensors from atomistic potentials and lattice structures. To address nonlocal interactions at the mesoscale, homogenization of a Representative Volume Element (RVE) is commonly employed. For instance, Drugan and Willis [41] and Drugan [42] extended the Hashin–Shtrikman variational formulation to derive micromechanics-based variational estimates for higher-order nonlocal constitutive equations in composites. Similarly, Geers et al. [43] and Kouznetsova et al. [44] developed a gradient-enhanced computational framework that generalizes classical homogenization to a fully gradient, geometrically nonlinear context, prescribing boundary conditions for a microstructural RVE using macroscopic deformation and its gradient. Yvonnet et al. [45] developed a computational homogenization method to determine the effective parameters of Mindlin’s strain gradient elasticity model from a local heterogeneous Cauchy linear material.

Among these efforts, two-scale asymptotic homogenization theory (also referred to as two-scale asymptotic expansion theory or mathematical homogenization theory) [46–48] has emerged as a mathematically rigorous multiscale framework for developing strain gradient models. For instance, Triantafyllidis and Bardenhagen [49] employed this method to express the critical load at the onset of the first instability in periodic solids in terms of the scale parameter ϵ and the higher-order gradient macroscopic modulus. Similarly, Smyshlyaev and Cheretnichenko [50] introduced a variational-asymptotic approach to derive higher-order constitutive relations for the scalar problem of antiplane shear, demonstrating its advantages over purely asymptotic methods, particularly when ϵ is “small but not too small”. Building on these foundations, Peerlings and Fleck [4] extended the approach to compute the strain gradient modulus in three-dimensional linear elasticity, exploring the derived parameters’ properties and showing that higher-order stiffness tensors gain importance as the stiffness contrast between inclusions and the matrix increases. Furthermore, Barboura and Li [51] investigated the mechanical implications, consistency, and strain energy convexity of strain gradient constitutive laws derived using this framework. In the dynamic context, Chen and Fish [52] developed a dispersive model for wave propagation in periodic heterogeneous media based on the higher order mathematical homogenization theory with multiple spatial and temporal scales. Bacigalupo and Gambarotta [53] and Bacigalupo and Gambarotta [26] derived the equations of motion for a second-order continuum equivalent to periodic masonry composed of deformable bricks and mortar. They employed a homogenization technique based on the variational-asymptotic approach of Smyshlyaev and Cheretnichenko [50] to evaluate the overall elastic moduli and inertial properties. Yang et al. [54] applied this methodology with a fitting procedure to study higher-order inertial parameters in dynamic strain gradient models. Complementing these studies in elasticity, Rao et al. [55,56] developed a unified damage and fracture model that integrates microstructural effects, strain gradients, and strain rates using two-scale asymptotic analysis alongside Griffith’s fracture criterion for brittle materials.

Beyond model construction and parameter determination, the mathematical foundations of strain gradient models present another significant challenge. The incorporation of higher-order strain and stress terms introduces additional complexity into the governing equations, complicating mathematical analyses [12]. A particular concern is the well-posedness of strain gradient models — specifically, the existence and uniqueness of solutions — which is not yet fully established, in sharp contrast to the classical theory of elasticity, where these foundational properties are firmly proven [47,57].

Progress has been made in the mathematical analysis of quasi-static strain gradient models. Notably, the sixth-order strain gradient stiffness tensor has been extensively studied, including its symmetry group classifications and explicit matrix representations [58–60]. Complete sets of matrices representing the fifth-order tensor, which arises in strain gradient elasticity models when the material’s microstructure lacks centrosymmetry, in each one of their anisotropic system are provided in [61,62]. In a variational framework, Niiranen et al. [63] formulated fourth-order boundary value problems for one-parameter gradient-elastic bar and plane strain/stress models within the H^2 Sobolev space, proving the existence and uniqueness of solutions by demonstrating the continuity and coercivity of the associated symmetric bilinear form. Similarly, Hosseini and Niiranen [13] analyzed the three-dimensional first strain gradient elasticity theory, deriving both continuous and discrete variational formulations and providing error estimates based on Sobolev space properties. For isotropic dilatational strain gradient elasticity, Eremeyev et al. [64] established an existence and uniqueness theorem for weak solutions to the equilibrium problem. Despite these advancements, a rigorous proof of the well-posedness of strain gradient elastodynamics model is still lack.

The present study aims to establish the well-posedness of a strain gradient elastodynamics model that is rigorously derived using the variational-asymptotic approach. Firstly, we derive the strain gradient elastodynamics equations for heterogeneous materials by employing first-order two-scale asymptotic expansion techniques combined with Hamilton’s variational principle. The model’s coefficients—the homogenized elasticity tensor C_{ijkl} , strain gradient stiffness tensor D_{ijklmn} , and micro-inertial tensor F_{ijkl} —are explicitly linked to the solutions of time-independent first-order cell problems. We demonstrate that the homogenized tensors C , D , and F are symmetric and positive definite. Furthermore, we provide the first proof of the general well-posedness of strain gradient elastodynamic models under the conditions of symmetry and positive definiteness of the coefficient tensors. This result applies not only to the present model but also to broader frameworks of strain gradient elastodynamics, such as those proposed by Mindlin [22], Aifantis [12], Bacigalupo and Gambarotta [53], Rosi and Auffray [27], Hosseini and Niiranen [13], and Yang et al. [54].

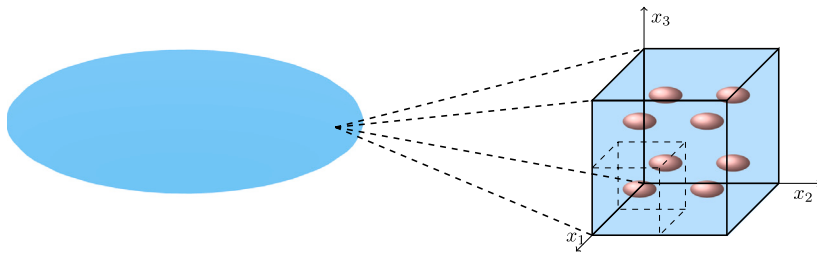


Fig. 1. Periodic microstructure in composite materials.

Finally, numerical simulations are conducted to validate the theoretical results and to illustrate the predictive capability of the strain gradient elastodynamics model in capturing the dynamic behavior of heterogeneous materials.

The present study aims to establish the well-posedness of a strain gradient elastodynamics model that is rigorously derived using the variational-asymptotic approach. Firstly, we derive the strain gradient elastodynamics equations for heterogeneous materials by employing first-order two-scale asymptotic expansion techniques combined with Hamilton's variational principle. The model's coefficients—the homogenized elasticity tensor C_{ijkl} , strain gradient stiffness tensor D_{ijklmn} , and micro-inertial tensor F_{ijkl} —are explicitly linked to the solutions of time-independent first-order cell problems. Notably, our model avoids the introduction of a slow temporal scale—as employed in [52]—or the necessity of a high-order formulation—as required in [53]. Therefore, compared to previous works, the present model is more concise and exhibits lower computational complexity. Secondly, we demonstrate that the homogenized tensors \mathbf{C} , \mathbf{D} , and \mathbf{F} are symmetric and positive definite. Furthermore, we provide the first proof of the general well-posedness of strain gradient elastodynamic models under the conditions of symmetry and positive definiteness of the coefficient tensors. This result applies not only to the present model but also to broader frameworks of strain gradient elastodynamics, such as those proposed by Mindlin [22], Aifantis [12], Bacigalupo and Gambarotta [53], Rosi and Auffray [27], Hosseini and Niiranen [13], and Yang et al. [54]. Finally, numerical simulations are conducted to validate the theoretical results and to illustrate the predictive capability of the strain gradient elastodynamics model in capturing the dynamic behavior of heterogeneous materials.

The remainder of the paper is organized as follows: Section 2 details the formulation of the static and dynamic homogenized strain gradient equations, Section 3 presents the mathematical proof of existence and uniqueness, and Section 4 offers numerical validations of the model's efficacy in predicting the mechanical behavior of composite materials. Throughout this paper the Einstein summation convention is adopted.

2. Modeling

2.1. Two-scale approximation of displacement

We consider the deformation of an elastic medium Ω containing periodically distributed microstructures, represented by a periodic Representative Volume Element (RVE) Y_ϵ with a small characteristic size ϵ , as illustrated in Fig. 1. The microscopic elastodynamics equations are given by:

$$\rho^\epsilon \ddot{u}_i - \frac{\partial \sigma_{ij}^\epsilon}{\partial x_j} = f_i; \quad \sigma_{ij}^\epsilon = a_{ijkl}^\epsilon e_{kl}(\mathbf{u}^\epsilon); \quad e_{kl}(\mathbf{u}^\epsilon) = \frac{1}{2} \left(\frac{\partial u_k^\epsilon}{\partial x_l} + \frac{\partial u_l^\epsilon}{\partial x_k} \right), \quad (1)$$

where \mathbf{u}^ϵ , $e_{ij}(\mathbf{u}^\epsilon)$, and σ^ϵ denote the displacement, strain, and stress fields, respectively. To ensure the well-posedness of the obtained strain gradient elastodynamic equations, we assume that the elastic modulus a_{ijkl}^ϵ is symmetric and positive definite:

$$\begin{aligned} a_{ijkl}^\epsilon &= a_{jikl}^\epsilon = a_{klij}^\epsilon, \\ \exists \alpha > 0, \quad a_{ijkl}^\epsilon m_{ij} m_{kl} &\geq \alpha \left(\sum_{i,j} m_{ij}^2 \right)^{1/2}, \quad \forall \mathbf{m} \in \mathbb{R}^{3 \times 3}, \quad m_{ij} = m_{ji}, \end{aligned} \quad (2)$$

which holds for general isotropic materials.

Through the scaling transformation $\mathbf{y} = \frac{\mathbf{x}}{\epsilon}$, the RVE can be mapped onto a unit reference cell $Y = [0, 1] \times [0, 1] \times [0, 1]$, as illustrated in Fig. 2. The elasticity tensor a_{ijkl}^ϵ (and similarly λ^ϵ and μ^ϵ) and the density ρ^ϵ are periodic functions, expressed as:

$$a^\epsilon(\mathbf{x}) = a \left(\frac{\mathbf{x}}{\epsilon} - \left\lfloor \frac{\mathbf{x}}{\epsilon} \right\rfloor \right), \quad \rho^\epsilon(\mathbf{x}) = \rho \left(\frac{\mathbf{x}}{\epsilon} - \left\lfloor \frac{\mathbf{x}}{\epsilon} \right\rfloor \right), \quad (3)$$

where a_{ijkl} and ρ are Y -periodic functions.

Based on two-scale asymptotic homogenization theory, the introduction of the two-scale variables \mathbf{x} and \mathbf{y} leads to a formal asymptotic expansion of \mathbf{u}^ϵ in the following form [47]:

$$\mathbf{u}^\epsilon(\mathbf{x}) = \mathbf{u}^{(0)}(\mathbf{x}, \mathbf{y}) + \epsilon \mathbf{u}^{(1)}(\mathbf{x}, \mathbf{y}) + \epsilon^2 \mathbf{u}^{(2)}(\mathbf{x}, \mathbf{y}) + \dots, \quad (4)$$

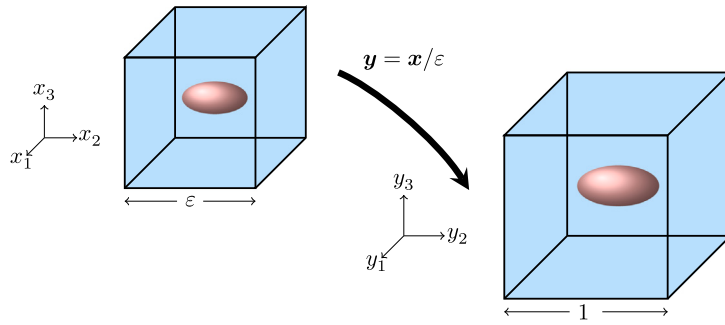


Fig. 2. Scale transformation.

where $\mathbf{u}^{(i)}(\mathbf{x}, \mathbf{y})$ are defined for $\mathbf{x} \in \Omega$ and $\mathbf{y} \in Y$, and are Y -periodic with respect to the microscopic variable \mathbf{y} .

The scale transformation implies the following chain rule for derivatives:

$$\frac{d}{dx} = \frac{\partial}{\partial x} + \frac{1}{\varepsilon} \frac{\partial}{\partial y}. \quad (5)$$

By substituting Eqs. (4) and (5) into Eq. (1) and equating the power-like terms of ε , one can obtain the following equations for $\mathbf{u}^{(0)}$ and $\mathbf{u}^{(1)}$:

$$\begin{cases} \frac{\partial}{\partial y_j} a_{ijkl} e_{ykl}(\mathbf{u}^{(0)}) = 0, & \text{in } Y, \\ \mathbf{u}^{(0)} \in D(Y); \end{cases} \quad (6)$$

$$\begin{cases} \frac{\partial}{\partial y_j} a_{ijkl} (e_{xkl}(\mathbf{u}^{(0)}) + e_{ykl}(\mathbf{u}^{(1)})) = 0, & \text{in } Y, \\ \mathbf{u}^{(1)} \in D(Y); \end{cases} \quad (7)$$

where the Sobolev space $D(Y)$ is defined as follows:

$$D(Y) = \left\{ \mathbf{u} | \mathbf{u} \in [H^1(Y)]^3, \mathbf{u} \text{ is } Y\text{-periodic, and } \int_Y \mathbf{u} d\mathbf{y} = \mathbf{0} \right\}.$$

It is demonstrated that the solutions of Eq. (6) are independent of \mathbf{y} , meaning that $\mathbf{u}^{(0)}(\mathbf{x}, \mathbf{y}) = \mathbf{u}^{(0)}(\mathbf{x})$ [46,47,65]. And the solutions of Eq. (7) have variable separation form:

$$\mathbf{u}^{(1)}(\mathbf{x}, \mathbf{y}) = \mathbf{N}^{pq}(\mathbf{y}) e_{xpq}(\mathbf{u}^{(0)})(\mathbf{x}) + \tilde{\mathbf{u}}^{(1)}(\mathbf{x}), \quad (8)$$

where $\mathbf{N}^{pq} \in D(Y)$ ($p, q \in \{1, 2, 3\}$) are the first-order cell functions satisfying the following governing equations:

$$\begin{cases} \frac{\partial}{\partial y_j} (a_{ijkl} e_{ykl}(\mathbf{N}^{pq}) + a_{ijpq}) = 0, & \text{in } Y, \\ \mathbf{N}^{pq} \in D(Y). \end{cases} \quad (9)$$

Note that, \mathbf{N}^{pq} are time-independent vector-valued functions with three components, denoted \mathbf{N}_i^{pq} , where $i = \{1, 2, 3\}$. In addition, $\tilde{\mathbf{u}}^{(1)}(\mathbf{x})$ represents integration constants. Before proceeding with further analysis, we first derive the governing equation for $\tilde{\mathbf{u}}^{(1)}(\mathbf{x})$. By substituting Eqs. (4) and (5) into Eq. (1) and collecting terms of order ε^0 and ε^1 , we obtain

$$\frac{\partial}{\partial x_j} a_{ijkl} (e_{xkl}(\mathbf{u}^{(0)}) + e_{ykl}(\mathbf{u}^{(1)})) + \frac{\partial}{\partial y_j} a_{ijkl} (e_{xkl}(\mathbf{u}^{(1)}) + e_{ykl}(\mathbf{u}^{(2)})) = \rho \ddot{u}_i - f_i, \quad \text{in } Y, \quad (10)$$

and

$$\frac{\partial}{\partial x_j} a_{ijkl} (e_{xkl}(\mathbf{u}^{(1)}) + e_{ykl}(\mathbf{u}^{(2)})) + \frac{\partial}{\partial y_j} a_{ijkl} (e_{xkl}(\mathbf{u}^{(2)}) + e_{ykl}(\mathbf{u}^{(3)})) = 0, \quad \text{in } Y. \quad (11)$$

According to Eq. (10), the solutions $\mathbf{u}^{(2)}$ have variable separation form:

$$\mathbf{u}^{(2)}(\mathbf{x}, \mathbf{y}) = \mathbf{N}^{pqr}(\mathbf{y}) e_{xptr}(\mathbf{u}^{(0)})(\mathbf{x}) + \mathbf{N}^{pq}(\mathbf{y}) e_{xpq}(\tilde{\mathbf{u}}^{(1)})(\mathbf{x}) + \tilde{\mathbf{u}}^{(2)}(\mathbf{x}). \quad (12)$$

By integrating Eq. (11) over the unit cell Y and using the fact that $\mathbf{u}^{(3)}$ is Y -periodic, we obtain the homogenized equation

$$\frac{\partial}{\partial x_j} \int_Y a_{ijkl} (e_{xkl}(\mathbf{u}^{(1)}) + e_{ykl}(\mathbf{u}^{(2)})) d\mathbf{y} = 0, \quad (13)$$

which can be rewritten as

$$\frac{\partial}{\partial x_j} \left(\int_Y a_{ijkl} + a_{ijpq} e_{ypq} (\mathbf{N}^{kl}) dy \right) e_{xkl}(\tilde{\mathbf{u}}^1) = - \left(\int_Y a_{ijkr} N_k^{pq} + a_{ijkl} e_{ykl} (\mathbf{N}^{pqr}) dy \right) \frac{\partial^3 u_p^{(0)}}{\partial x_q \partial x_r \partial x_l}. \quad (14)$$

This equation indicates that the calculation of $\tilde{\mathbf{u}}^{(1)}$ requires the second-order cell functions and involves the third-order gradient of the macroscopic displacement $\mathbf{u}^{(0)}$, i.e., the second-order strain gradient. Since our primary focus is on the first-order strain gradients (i.e., second-order displacement gradient), we neglect $\tilde{\mathbf{u}}^{(1)}$ in following derivations. In fact, similar simplification, i.e., to neglect influence of $\tilde{\mathbf{u}}^{(1)}$, has been demonstrated to be acceptable in various asymptotic homogenization methods, including both traditional approaches [65,66] and variational asymptotic homogenization techniques [67,68], as well as their extended applications [55,56,69].

Therefore, we take the first order two-scale approximation of $\mathbf{u}^\varepsilon(\mathbf{x})$ as:

$$\mathbf{u}^\varepsilon(\mathbf{x}) \approx \mathbf{u}^{(0)}(\mathbf{x}) + \varepsilon \mathbf{N}^{pq} \left(\frac{\mathbf{x}}{\varepsilon} \right) e_{xpq} (\mathbf{u}^{(0)}) (\mathbf{x}), \quad (15)$$

where $\mathbf{u}^{(0)}$ represent the leading-order approximation, and $\mathbf{N}^{pq}(\mathbf{y})$ account for the non-local effects of the microstructure.

2.2. Two-scale approximation of homogenized energy density functions

In order to construct a homogenized elastodynamics model, here we firstly derive the expressions for the homogenized strain energy and kinetic energy density functions based on the two-scale asymptotic homogenization theory.

From Eq. (15), the approximation of the local strain in the micro-scale RVE is given by:

$$e_{ij}(\mathbf{u}^\varepsilon) \approx e_{xij} (\mathbf{u}^{(0)}) + e_{yij} (\mathbf{N}^{pq}) e_{xpq} (\mathbf{u}^{(0)}) + \frac{\varepsilon}{2} \left(\mathbf{N}_i^{pq} \frac{\partial e_{xpq} (\mathbf{u}^{(0)})}{\partial x_j} + \mathbf{N}_j^{pq} \frac{\partial e_{xpq} (\mathbf{u}^{(0)})}{\partial x_i} \right). \quad (16)$$

Based on the symmetry of a_{ijkl} , we obtain the local strain energy density W^ε as:

$$\begin{aligned} W^\varepsilon(\mathbf{x}) &= \frac{1}{2} a_{ijkl} e_{ij}(\mathbf{u}^\varepsilon) e_{kl}(\mathbf{u}^\varepsilon) \\ &\approx \frac{1}{2} a_{ijkl} e_{xij} (\mathbf{u}^{(0)}) e_{xkl} (\mathbf{u}^{(0)}) + \frac{1}{2} a_{ijkl} \mathbf{N}_{i,j}^{pq} \mathbf{N}_{k,l}^{mn} e_{xpq} (\mathbf{u}^{(0)}) e_{xmn} (\mathbf{u}^{(0)}) + a_{ijkl} \mathbf{N}_{i,j}^{pq} e_{xpq} (\mathbf{u}^{(0)}) e_{xkl} (\mathbf{u}^{(0)}) \\ &\quad + \varepsilon a_{ijkl} \left(e_{xij} (\mathbf{u}^{(0)}) + \mathbf{N}_{i,j}^{pq} e_{xpq} (\mathbf{u}^{(0)}) \right) \mathbf{N}_k^{mn} \frac{\partial e_{xmn} (\mathbf{u}^{(0)})}{\partial x_l} \\ &\quad + \frac{\varepsilon^2}{2} a_{ijkl} \mathbf{N}_i^{pq} \mathbf{N}_k^{mn} \frac{\partial e_{xpq} (\mathbf{u}^{(0)})}{\partial x_j} \frac{\partial e_{xmn} (\mathbf{u}^{(0)})}{\partial x_l}. \end{aligned}$$

The homogenized strain energy density W is calculated by volume averaging of W^ε over the RVE Y_ε :

$$\begin{aligned} W &= \frac{1}{|Y_\varepsilon|} \int_{Y_\varepsilon} W^\varepsilon(\mathbf{x}) d\mathbf{x} \\ &\approx \frac{\varepsilon^{-3}}{2} \langle e_{xij} (\mathbf{u}^{(0)}) \rangle \langle e_{xkl} (\mathbf{u}^{(0)}) \rangle \int_{Y_\varepsilon} a_{ijkl} d\mathbf{x} + \varepsilon^{-3} \langle e_{xpq} (\mathbf{u}^{(0)}) \rangle \langle e_{xkl} (\mathbf{u}^{(0)}) \rangle \int_{Y_\varepsilon} a_{ijkl} \mathbf{N}_{i,j}^{pq} \left(\frac{\mathbf{x}}{\varepsilon} \right) d\mathbf{x} \\ &\quad + \varepsilon^{-2} \langle e_{xpq} (\mathbf{u}^{(0)}) \rangle \langle \frac{\partial e_{xmn} (\mathbf{u}^{(0)})}{\partial x_l} \rangle \int_{Y_\varepsilon} (a_{pqkl} + a_{ijkl} \mathbf{N}_{i,j}^{pq}) \mathbf{N}_k^{mn} d\mathbf{x} \\ &\quad + \frac{\varepsilon^{-1}}{2} \left\langle \frac{\partial e_{xpq} (\mathbf{u}^{(0)})}{\partial x_j} \right\rangle \left\langle \frac{\partial e_{xmn} (\mathbf{u}^{(0)})}{\partial x_l} \right\rangle \int_{Y_\varepsilon} a_{ijkl} \mathbf{N}_i^{pq} \left(\frac{\mathbf{x}}{\varepsilon} \right) \mathbf{N}_k^{mn} \left(\frac{\mathbf{x}}{\varepsilon} \right) d\mathbf{x}, \end{aligned} \quad (17)$$

where $\langle \cdot \rangle = 1/|Y_\varepsilon| \int_{Y_\varepsilon} \cdot d\mathbf{x} = 1/\varepsilon^3 \int_{Y_\varepsilon} \cdot dy$ represents volume average over Y_ε . In deriving Eq. (17), the derivatives of $\mathbf{u}^{(0)}$ are approximated as constants (their volume averages), neglecting their slow variation over Y_ε [55,56]. And the following equality (which results from the variational formulation of Eq. (9)) is adopted:

$$\frac{\varepsilon^{-3}}{2} \int_{Y_\varepsilon} (a_{klpq} + a_{klji} \mathbf{N}_{i,j}^{pq}) \mathbf{N}_{k,l}^{mn} d\mathbf{x} = \frac{1}{2} \int_Y (a_{klpq} + a_{klji} e_{yij} (\mathbf{N}^{pq})) e_{ykl} (\mathbf{N}^{mn}) dy = 0. \quad (18)$$

Noting $\mathbf{y} = \frac{\mathbf{x}}{\varepsilon}$, Eq. (17) can be rewritten as:

$$W = \frac{1}{2} C_{ijkl} \mathcal{E}_{ij} \mathcal{E}_{kl} + \varepsilon G_{ijklm} \mathcal{E}_{ij} \mathcal{E}_{klm} + \frac{\varepsilon^2}{2} D_{ijklmn} \mathcal{E}_{ij,k} \mathcal{E}_{lm,n}, \quad (19)$$

where $\mathcal{E}_{ij} = \langle e_{xij} (\mathbf{u}^{(0)}) \rangle$, $\mathcal{E}_{ij,k} = \left\langle \frac{\partial e_{xij} (\mathbf{u}^{(0)})}{\partial x_k} \right\rangle$ represent the homogenized strain and strain gradient. And C_{ijkl} , G_{pqmn} and D_{pqjmnl} represent the homogenized material parameters related to the first-order cell functions:

$$C_{ijkl} = \int_Y a_{ijkl}(\mathbf{y}) + a_{ijpq}(\mathbf{y}) e_{xpq}(\mathbf{N}^{kl})(\mathbf{y}) dy, \quad (20)$$

$$G_{pqmn} = \int_Y (a_{pqkl}(\mathbf{y}) + a_{ijkl}(\mathbf{y}) \mathbf{N}_{i,j}^{pq}(\mathbf{y})) \mathbf{N}_k^{mn}(\mathbf{y}) dy, \quad (21)$$

$$D_{pqjml} = \int_Y a_{ijkl}(\mathbf{y}) \mathbf{N}_i^{pq}(\mathbf{y}) \mathbf{N}_k^{mn}(\mathbf{y}) d\mathbf{y}. \quad (22)$$

Following a similar procedure, we obtain the homogenized kinetic energy density function as:

$$\begin{aligned} K &= \frac{1}{|Y_\epsilon|} \int_{Y_\epsilon} \frac{1}{2} \rho \frac{\partial \mathbf{u}^\epsilon}{\partial t} \frac{\partial \mathbf{u}^\epsilon}{\partial t} d\mathbf{x} \\ &\approx \frac{1}{2} \left\langle \frac{\partial u_i^{(0)}}{\partial t} \right\rangle \left\langle \frac{\partial u_i^{(0)}}{\partial t} \right\rangle \int_Y \rho(\mathbf{y}) d\mathbf{y} + \epsilon \left\langle \frac{\partial e_{xij}(\mathbf{u}^{(0)})}{\partial t} \right\rangle \left\langle \frac{\partial u_k^{(0)}}{\partial t} \right\rangle \int_Y \rho(\mathbf{y}) \mathbf{N}_k^{ij}(\mathbf{y}) d\mathbf{y} \\ &\quad + \frac{\epsilon^2}{2} \left\langle \frac{\partial e_{xij}(\mathbf{u}^{(0)})}{\partial t} \right\rangle \left\langle \frac{\partial e_{xkl}(\mathbf{u}^{(0)})}{\partial t} \right\rangle \int_Y \rho(\mathbf{y}) \mathbf{N}_p^{ij}(\mathbf{y}) \mathbf{N}_p^{kl}(\mathbf{y}) d\mathbf{y} \\ &= \frac{1}{2} \hat{\rho} \dot{u}_i \dot{u}_i + \epsilon H_{ijk} \dot{u}_k \dot{\mathcal{E}}_{ij} + \frac{\epsilon^2}{2} F_{ijkl} \dot{\mathcal{E}}_{ij} \dot{\mathcal{E}}_{kl}, \end{aligned} \quad (23)$$

where $\dot{u}_i = \left\langle \frac{\partial u_i^{(0)}}{\partial t} \right\rangle$, $\dot{\mathcal{E}}_{ij} = \left\langle \frac{\partial e_{xij}(\mathbf{u}^{(0)})}{\partial t} \right\rangle$ represent the homogenized velocity and strain rate respectively. And $\hat{\rho}$, H_{ijk} and F_{ijkl} represent the homogenized material parameters:

$$\hat{\rho} = \int_Y \rho(\mathbf{y}) d\mathbf{y}, \quad (24)$$

$$H_{ijk} = \int_Y \rho(\mathbf{y}) \mathbf{N}_k^{ij}(\mathbf{y}) d\mathbf{y}, \quad (25)$$

$$F_{ijkl} = \int_Y \rho(\mathbf{y}) \mathbf{N}_p^{ij}(\mathbf{y}) \mathbf{N}_p^{kl}(\mathbf{y}) d\mathbf{y}. \quad (26)$$

The strain and kinetic energy density functions as formulated in Eqs. (19) and (23) are consistent with those reported by Rosi and Auffray [27]. For centrosymmetric inclusions, we prove that all components of \mathbf{G} and \mathbf{H} vanish (as detailed in Appendix B), which aligns with the findings of Mindlin [22] and Rosi and Auffray [27]. Given that centrosymmetry is commonly satisfied in microstructures, the terms related to \mathbf{G} and \mathbf{H} are typically neglected in strain gradient models. In the present work, we also disregard the contribution of the terms related to \mathbf{G} and \mathbf{H} , simplifying the strain and kinetic energy density functions as follows:

$$W = \frac{1}{2} C_{ijkl} \mathcal{E}_{ij} \mathcal{E}_{kl} + \frac{\epsilon^2}{2} D_{ijklmn} \mathcal{E}_{ij,k} \mathcal{E}_{lm,n}, \quad (27)$$

$$K = \frac{1}{2} \hat{\rho} \dot{u}_i \dot{u}_i + \frac{\epsilon^2}{2} F_{ijkl} \dot{\mathcal{E}}_{ij} \dot{\mathcal{E}}_{kl},. \quad (28)$$

The symmetries of the tensors \mathbf{C} , \mathbf{D} , and \mathbf{F} can be derived from their definitions (Eqs. (20), (22), (26)) as follows:

$$C_{ijkl} = C_{jikl} = C_{klij}, \quad D_{ijklmn} = D_{jiklmn} = D_{lmnijk}, \quad F_{ijkl} = F_{jikl} = F_{klij}. \quad (29)$$

Thus, in the case of triclinic anisotropy, the tensors \mathbf{C} , \mathbf{D} , and \mathbf{F} contain 21, 171, and 21 independent components, respectively. However, when materials exhibit specific symmetry properties, the number of independent components decreases accordingly. This reduction is a consequence of the symmetry of the first-order cell functions, as detailed in Appendix B. For example, in the case of heterogeneous materials with orthotropic inclusions— π -invariant about each axis—the number of independent components for \mathbf{C} , \mathbf{D} , and \mathbf{F} reduces to 9, 51, and 9, respectively. In the case of cubic symmetry, which imposes even higher symmetry on the microstructure—invariant under the permutation of $\{y_1, y_2, y_3\}$ —the number of independent components is further reduced to 3, 11, and 3, respectively. These results are consistent with the theoretical results presented in [58–60].

2.3. Governing equations of strain gradient elastodynamics

We derive the homogenized strain gradient equations using Hamilton's principle, based on the homogenized strain and kinetic energy density functions obtained in Section 2.2.

Hamilton's principle applied to the homogenized medium Ω is expressed as:

$$\delta \int_{t_0}^{t_1} \int_{\Omega} (K - W) d\mathbf{x} dt + \delta \int_{t_0}^{t_1} \mathcal{W}^{ext} dt = 0, \quad (30)$$

where \mathcal{W}^{ext} stands for the work done by the external forces.

By applying the divergence theorem, the variation of the total kinetic energy (as defined in Eq. (28)) can be expressed as:

$$\begin{aligned} \delta \int_{t_0}^{t_1} \int_{\Omega} K d\mathbf{x} dt &= \int_{t_0}^{t_1} \frac{\partial K}{\partial \dot{u}_i} \delta \dot{u}_i + \frac{\partial K}{\partial \dot{\mathcal{E}}_{ij}} \delta \dot{\mathcal{E}}_{ij} dt \\ &= - \int_{t_0}^{t_1} \int_{\Omega} \rho \dot{u}_i \delta \dot{u}_i - \epsilon^2 F_{ijkl} \dot{\mathcal{E}}_{kl,j} \delta u_i d\mathbf{x} dt - \int_{t_0}^{t_1} \int_{\partial\Omega} \epsilon^2 F_{ijkl} \left(\frac{\partial \dot{u}_l}{\partial x_k} \right) n_j \delta u_i dS. \end{aligned} \quad (31)$$

To address the variation of strain energy, we first define the stress tensor Σ_{ij} and the double stress tensor Γ_{ijk} as the energy conjugates of the strain and its gradient, respectively:

$$\Sigma_{ij} = \frac{\partial W}{\partial \mathcal{E}_{ij}} = C_{ijkl} \mathcal{E}_{kl}, \quad \Gamma_{ijk} = \frac{\partial W}{\partial \mathcal{E}_{ijk,k}} = \epsilon^2 D_{ijklmn} \mathcal{E}_{lm,n}. \quad (32)$$

These are referred to as higher-order effective constitutive relations.

Next, we define the surface gradient operator D_j , and normal gradient operator D as:

$$D_j = (\delta_{jk} - n_j n_k) \frac{\partial}{\partial x_k}, \quad D = n_k \frac{\partial}{\partial x_k}, \quad (33)$$

where \mathbf{n} is the unit outer normal on $\partial\Omega$. The boundary surface $\partial\Omega$ is assumed to be divisible into a finite number of smooth parts S_n , each bounded by an edge C_n , with a surface unit vector k_n normal to the edge. Then, by applying the Green's divergence theorem and Stokes' surface divergence theorem, the variation of the total strain energy (as defined in Eq. (27)) is given by:

$$\begin{aligned} \delta \int_{t_0}^{t_1} \int_{\Omega} W dx dt &= \int_{t_0}^{t_1} \int_{\Omega} \Sigma_{ij} \delta \mathcal{E}_{ij} + \Gamma_{ijk} \delta \mathcal{E}_{ijk} dx dt \\ &= - \int_{\Omega} \left(\frac{\partial}{\partial x_i} \Sigma_{ik} - \frac{\partial^2}{\partial x_i \partial x_j} \Gamma_{ijk} \right) \delta u_k dx \\ &\quad + \int_{\partial\Omega} \left\{ \left[n_j (\Sigma_{ij} - \frac{\partial \Gamma_{ijk}}{\partial x_i}) + n_i n_j \Gamma_{ijk} (D_l n_l) - D_j (n_i \Gamma_{ijk}) \right] \delta u_k + n_i n_j \Gamma_{ijk} D \delta u_k \right\} dS \\ &\quad + \sum_m \oint_{C_m} [n_i k_j \Gamma_{ijk}] \delta u_k ds, \end{aligned} \quad (34)$$

where m is the number of sharp edges, and $[\cdot]$ represents the difference between the bracketed terms on the two sides of the edge [3]. The expression for the variation of work done by external forces is given by:

$$\delta \mathcal{W}^{ext} = \int_{\Omega} f_k \delta u_k dx + \int_{\partial\Omega} g_k \delta u_k dS + \int_{\partial\Omega} r_k D(\delta u_k) dS + \sum_m \oint_{C_m} p_k \delta u_k ds. \quad (35)$$

Thus, by taking Eqs. (31)–(35) into Eq. (30), and noting arbitrariness of the virtual displacement $\delta \mathbf{u}$, we obtain the governing equations of the strain gradient elastodynamics:

$$\begin{cases} \hat{\rho} \ddot{u}_i - \epsilon^2 F_{ijkl} \ddot{\mathcal{E}}_{kl,j} - \frac{\partial}{\partial x_j} (\Sigma_{ij}) + \epsilon^2 \frac{\partial^2}{\partial x_k \partial x_j} (\Gamma_{ijk}) = f_i, & \text{in } \Omega, \\ \mathbf{u} = \bar{\mathbf{u}} \text{ or } n_j (\Sigma_{ij} - \frac{\partial \Gamma_{ijk}}{\partial x_i}) + n_i n_j \Gamma_{ijk} (D_l n_l) - D_j (n_i \Gamma_{ijk}) + \epsilon^2 F_{ijkl} \left(\frac{\partial \ddot{u}_i}{\partial x_j} \right) n_l = g_k, & \text{on } \partial\Omega, \\ \frac{\partial \mathbf{u}}{\partial n} = \frac{\partial \bar{\mathbf{u}}}{\partial n} \text{ or } n_i n_j \Gamma_{ijk} = r_i, & \text{on } \partial\Omega, \\ \mathbf{u} = \bar{\mathbf{u}} \text{ or } [n_i k_j \Gamma_{ijk}] = p_k, & \text{on } C_m, \\ \mathbf{u}|_{t=0} = \mathbf{u}_0, \quad \dot{\mathbf{u}}|_{t=0} = \mathbf{u}_1, & \text{in } \Omega. \end{cases} \quad (36)$$

Ignoring time derivative-related items, we also derive the governing equations for strain gradient static elasticity:

$$\begin{cases} -\frac{\partial}{\partial x_j} (\Sigma_{ij}) + \epsilon^2 \frac{\partial^2}{\partial x_k \partial x_j} (\Gamma_{ijk}) = f_i, & \text{in } \Omega, \\ \mathbf{u} = \bar{\mathbf{u}} \text{ or } n_j (\Sigma_{ij} - \frac{\partial \Gamma_{ijk}}{\partial x_i}) + n_i n_j \Gamma_{ijk} (D_l n_l) - D_j (n_i \Gamma_{ijk}) = g_k, & \text{on } \partial\Omega, \\ \frac{\partial \mathbf{u}}{\partial n} = \frac{\partial \bar{\mathbf{u}}}{\partial n} \text{ or } n_i n_j \Gamma_{ijk} = r_k, & \text{on } \partial\Omega, \\ \mathbf{u} = \bar{\mathbf{u}} \text{ or } [n_i k_j \Gamma_{ijk}] = p_k, & \text{on } C_m. \end{cases} \quad (37)$$

Remark 1. We noted that [26,52,53] employed variational-asymptotic techniques to establish strain gradient elastodynamics models for periodic heterogeneous media. Our proposed model offers a simplified framework, avoiding the introduction of a slow temporal scale, as in [52], and high-order unit cell functions, as in [53]. Additionally, unlike the model in [26], which conducts an asymptotic expansion in the frequency domain, our method directly performs the asymptotic expansion in the physical time domain. In the present work, the homogenized coefficients (\mathbf{C} , \mathbf{D} , and \mathbf{F}) are obtained by integrating time-independent first-order cell functions, which can be efficiently computed by solving Eq., (9). Thus this simplified approach significantly reduces computational cost.

Remark 2. From the early 1990s, Aifantis and co-workers proposed a simplified version of the Mindlin's strain gradient model. For dynamic problems, they use only two length parameters to construct the strain gradient stiffness tensor \mathbf{D} and the micro-inertial tensor \mathbf{F} [12,70–74]. The corresponding dynamic strain gradient equations are expressed as follows:

$$\hat{\rho} \ddot{u}_i - \hat{\rho} l_d^2 \ddot{\mathcal{E}}_{im,m} - \frac{\partial}{\partial x_j} (C_{ijkl} \mathcal{E}_{kl}) + \frac{\partial^2}{\partial x_k \partial x_j} (l_s^2 C_{ijlm} \delta_{kn} \mathcal{E}_{lm,n}) = f_i, \quad (38)$$

where l_s and l_d are referred to as internal length, internal inertia, respectively.

By comparing the coefficients of Eqs. (36a) and (38), we can estimate the homogenized internal length l_s and the homogenized internal inertia l_d as follows:

$$\begin{aligned} l_s &= \arg \min_l \sum_{ijklmn} \|\varepsilon^2 D_{ijklmn} - l^2 C_{ijlm} \delta_{kn}\|^2 = \varepsilon \sqrt{\frac{\sum_{ijklmn} D_{ijklmn} C_{ijlm} \delta_{kn}}{\sum_{ijklmn} (C_{ijlm} \delta_{kn})^2}} = \varepsilon L_s, \\ l_d &= \arg \min_l \sum_{ijkl} \|\varepsilon^2 F_{ijkl} - l^2 \hat{\rho} \delta_{ik} \delta_{lj}\|^2 = \arg \min_l \sum_{ij} \|\varepsilon^2 F_{ijij} - l^2 \hat{\rho}\|^2 = \varepsilon \sqrt{\sum_{ijkl} \frac{F_{ijkl}}{\hat{\rho}}} = \varepsilon L_d. \end{aligned} \quad (39)$$

In Eq. (39), L_s and L_d denote the normalized homogenized internal length and normalized homogenized internal inertia, respectively. These quantities are determined by the first-order cell functions, which capture the inhomogeneity of the microstructure. Meanwhile, ε denotes the side length of the reference cell, which characterizes the scale of the microstructure.

3. Well-posedness of the strain gradient elastodynamics model

3.1. Proving the positive definiteness of $\mathbf{C}, \mathbf{D}, \mathbf{F}$

In this subsection, we prove the positive definiteness of $\mathbf{C}, \mathbf{D}, \mathbf{F}$: there exist $0 < \alpha_1 < \beta_1, 0 < \alpha_2 < \beta_2, 0 < \alpha_3 < \beta_3$, such that for arbitrary strain tensor $\mathbf{m} \in \text{sym}(\mathcal{R}^{3 \times 3})$ and strain gradient tensor $\eta \in \text{sym}(\mathcal{R}^{3 \times 3 \times 3})$:

$$m_{ij} C_{ijkl} m_{kl} \geq \alpha_1 \|\mathbf{m}\|_F^2, \quad |\mathbf{C} : \mathbf{m}|_F \leq \beta_1 \|\mathbf{m}\|_F, \quad (40a)$$

$$m_{ij} F_{ijkl} m_{kl} \geq \alpha_2 \|\mathbf{m}\|_F^2, \quad |\mathbf{F} : \mathbf{m}|_F \leq \beta_2 \|\mathbf{m}\|_F, \quad (40b)$$

$$\eta_{ijk} D_{ijklmn} \eta_{lmn} \geq \alpha_3 \|\eta\|_F^2, \quad |\mathbf{D} : \eta|_F \leq \beta_3 \|\eta\|_F, \quad (40c)$$

where $\text{sym}(\mathcal{R}^{3 \times 3}) = \{\mathbf{m} \in \mathcal{R}^{3 \times 3} | m_{ij} = m_{ji}\}$, $\text{sym}(\mathcal{R}^{3 \times 3 \times 3}) = \{\eta \in \mathcal{R}^{3 \times 3 \times 3} | \eta_{ijk} = \eta_{jik}\}$, and $\|\cdot\|_F$ denotes the Frobenius norm of a matrix or tensor, defined as:

$$\|\mathbf{A}\|_F = \sqrt{\sum_{i,j} a_{ij}^2} \quad (41)$$

for a matrix $\mathbf{A} = (a_{ij})$, and similarly for higher-order tensors.

Firstly, the elastic tensor $(\mathbf{A})_{ijkl} = a_{ijkl}$ is positive definite, meaning that there exist constants $0 < \alpha_0 < \beta_0$ such that for all $\mathbf{m} \in \text{sym}(\mathcal{R}^{3 \times 3})$ and $\mathbf{y} \in Y$, the following inequalities hold:

$$\alpha_0 \|\mathbf{m}\|_F^2 \leq a_{ijkl}(\mathbf{y}) m_{ij} m_{kl}, \quad |\mathbf{A}(\mathbf{y}) : \mathbf{m}|_F \leq \beta_0 \|\mathbf{m}\|_F \quad (42)$$

Based on this property (Eq. (42)), the proof of the positive definiteness of \mathbf{C} , as expressed in Eq. (40a), is provided in Chapter 10 of Cioranescu and Donato [66].

Proof of the positive definiteness of \mathbf{F} , Eq. (40b). From the definition of \mathbf{F} (Eq. (26)), we have

$$m_{ij} F_{ijkl} m_{kl} = \int_Y \rho(\mathbf{y}) m_{ij} N_p^{ij}(\mathbf{y}) m_{kl} N_p^{kl}(\mathbf{y}) d\mathbf{y}. \quad (43)$$

Since $\rho > 0$, and $m_{ij} N_p^{ij} \neq 0, \forall \mathbf{m} \neq 0 \in \text{sym}(\mathcal{R}^{3 \times 3})$ (according to Lemma 1 in Appendix D), we obtain that:

$$m_{ij} F_{ijkl} m_{kl} = \int_Y \rho m_{ij} N_p^{ij} m_{kl} N_p^{kl} d\mathbf{y} > 0, \quad \forall \mathbf{m} \neq 0 \in \text{sym}(\mathcal{R}^{3 \times 3}). \quad (44)$$

Define $\psi(\mathbf{m}) = m_{ij} F_{ijkl} m_{kl}$. Since ψ is continuous on the compact set $S = \{\mathbf{m} \in \text{sym}(\mathcal{R}^{3 \times 3}) | \|\mathbf{m}\|_F = 1\}$, by the extreme value theorem,¹ ψ reaches its minimum at some point $\mathbf{m}^* \in S$. From Eq. (40b), we have $\psi(\mathbf{m}^*) > 0$. Therefore, for any $\mathbf{m} \neq 0 \in \text{sym}(\mathcal{R}^{3 \times 3})$, $\psi\left(\frac{\mathbf{m}}{\|\mathbf{m}\|_F}\right) \geq \psi(\mathbf{m}^*) > 0$, i.e.,

$$\frac{m_{ij}}{\|\mathbf{m}\|_F} F_{ijkl} \frac{m_{kl}}{\|\mathbf{m}\|_F} \geq \psi(\mathbf{m}^*), \quad (45)$$

So Eq. (40b) is proved by taking $\alpha_2 = \psi(\mathbf{m}^*)$.

The positive definiteness of \mathbf{D} , Eq. (40c), can be proven in a manner analogous to that of \mathbf{F} .

Remark 3. Note that the tensors $\mathbf{C}, \mathbf{D}, \mathbf{F}$ can be written in their corresponding Voigt forms as 6×6 , 18×18 , and 6×6 matrices, respectively (as shown in Fig. B.1). The definition of positive definiteness in Eqs. (40a) to (40b) and the symmetry conditions in Eq. (29) are thus equivalent to the symmetric positive definiteness of the Voigt matrices. Specifically, this means that all eigenvalues of the Voigt matrices must be real and strictly positive.

¹ A continuous function can reach its minimum on a compact set.

3.2. Proving the well-posedness of strain gradient elastodynamics model

Assume that Ω is convex with a Lipschitz continuous boundary $\partial\Omega$. For simplicity, the homogenized strain gradient elastodynamics equations are formulated in variational form within a Sobolev space framework, subject to the following homogeneous boundary conditions, commonly referred to as clamped boundary conditions:

$$\mathbf{u} = \frac{\partial \mathbf{u}}{\partial \mathbf{n}} = 0, \text{ on } \partial\Omega. \quad (46)$$

We then establish the existence and uniqueness of the homogenized elastodynamics solutions, along with the symmetric positive definiteness of the coefficient tensors. These results can be naturally extended to more general cases including non-homogeneous boundary conditions.

In what follows, we will adopt the following notation:

$$\begin{aligned} H_0^1(\Omega) &= \{v \in H^1(\Omega) | v = 0 \text{ on } \partial\Omega\}, \quad H_0^2(\Omega) = \{v \in H^2(\Omega) | v = \frac{\partial v}{\partial \mathbf{n}} = 0 \text{ on } \partial\Omega\} \\ \mathcal{W} &= \{v \in L^2(a, b; H_0^2), \frac{\partial v}{\partial t} \in L^2(a, b; H^1(\Omega))\}, \end{aligned}$$

where $H^s(\Omega)$ denotes the Sobolev space of order s , consisting of square-integrable real-valued functions defined on Ω with square-integrable weak derivatives up to order s . The corresponding Sobolev norm and seminorm are denoted by $\|\cdot\|_s$ and $|\cdot|_s$, respectively.

The variational form of the dynamic strain gradient equations, Eq. (36a), is then given by:

$$\left\{ \begin{array}{l} \text{Find } \mathbf{u} \in (\mathcal{W})^3 \text{ such that :} \\ \int_{\Omega} \hat{\rho} \bar{\mathbf{u}} \mathbf{v} d\mathbf{x} + \int_{\Omega} \epsilon^2 F_{ijkl} e_{ij}(\bar{\mathbf{u}}) e_{kl}(\mathbf{v}) + a(\mathbf{u}, \mathbf{v}) = l(\mathbf{v}) \quad \text{in } D'(0, T), \forall \mathbf{v} \in (H_0^2(\Omega))^3, \quad (\text{a}) \\ \mathbf{u}(0) = \mathbf{u}_0 \quad \text{in } (H_0^2(\Omega))^3 \quad (\text{b}) \\ \dot{\mathbf{u}}(0) = \mathbf{u}_1 \quad \text{in } (H^1(\Omega))^3 \quad (\text{c}) \end{array} \right. \quad (47)$$

where the bilinear form $a : (H_0^2(\Omega))^3 \times (H_0^2(\Omega))^3 \rightarrow \mathbb{R}$ and the load functional $l : (H_0^2(\Omega))^3 \rightarrow \mathbb{R}$, respectively, are defined as

$$a(\mathbf{u}, \mathbf{v}) = \int_{\Omega} \frac{1}{2} C_{ijkl} e_{ij}(\mathbf{u}) e_{kl}(\mathbf{v}) + \epsilon^2 D_{ijklmn} e_{ijk}(\mathbf{u}) e_{lmn}(\mathbf{v}) d\mathbf{x} \quad (48)$$

$$l(\mathbf{v}) = \int_{\Omega} f_i v_i d\mathbf{x}. \quad (49)$$

Based on the positive definiteness of $\mathbf{C}, \mathbf{D}, \mathbf{F}$, we can prove that: *for a given loading $\mathbf{f} \in (H^{-2}(\Omega))^3$, init displacement $\mathbf{u}^0 \in (H_0^2(\Omega))^3$, init velocity $\mathbf{u}^1 \in (H_0^1(\Omega))^3$, Eq. (47) has a unique solution in \mathcal{W}^3 .* The process of proof is also presented in Appendix D.

Remark 4. It is important to note that this conclusion is not only valid for the model presented in this paper but also for general strain gradient models, provided that the coefficient tensors $\mathbf{C}, \mathbf{D}, \mathbf{F}$ satisfy the symmetry conditions in Eq. (29) and the positive definiteness conditions in Eqs. (40a)–(40b). In such cases, the corresponding strain gradient model is well-posed.

Since the elastic modulus C_{ijkl} is symmetric and positive definite, the terms $l^2 C_{ijkl} \delta_{kn}$ and $l^2 \hat{\rho} \delta_{ik} \delta_{lj}$ in the two-parameter dynamic strain gradient model (Eq. (38)), which approximate D_{ijklmn} and F_{ijkl} , also satisfy the conditions of symmetric positive definiteness. This ensures the existence and uniqueness of solutions, as inferred from the preceding results.

4. Numerical results

In this section, we present numerical results on the dependence of \mathbf{C} , \mathbf{D} , and \mathbf{F} on microstructural features and macrostructural responses (including vibration, tension, impact, and wave dispersion) to demonstrate the capabilities of the proposed model in capturing dynamic behaviors of heterogeneous materials and structures. We compare the numerical results obtained from the strain gradient elastodynamics model with classical elastodynamic solutions in terms of stress singularities, mesh sensitivity, and wave dispersion.

In all the numerical examples, we assume isotropic elasticity:

$$a_{ijkl}^e(\mathbf{x}) = \lambda^e(\mathbf{x}) \delta_{ij} \delta_{kl} + \mu^e(\mathbf{x}) (\delta_{ik} \delta_{jl} + \delta_{il} \delta_{jk}), \quad (50)$$

where λ^e and μ^e are the Lamé parameters, and δ_{ij} is the Kronecker delta symbol.

4.1. Dependence of \mathbf{C} , \mathbf{D} , and \mathbf{F} on microstructure features

The first-order cell functions \mathbf{N}^{pq} are obtained by solving Eq. (9) through finite element simulations utilizing tetrahedral meshes. In this work, the $\text{ZrO}_2/\text{Ti-C6Al-C4V}$ composite is selected as the material system for investigation. The matrix material is ZrO_2 , with a Ti-C6Al-C4V inclusion positioned at the center of the RVE. The material properties of ZrO_2 and Ti-C6Al-C4V are provided in Table 1.

Table 1
Material properties of the composite.

Property	ZrO_2 (Matrix)	$TiC6AlC4V$ (Inclusion)
Young's modulus, E (Pa)	117.0×10^9	66.2×10^9
Poisson's ratio, ν	0.333	0.321
Density, ρ (kg/m ³)	5.6×10^3	4.41×10^3

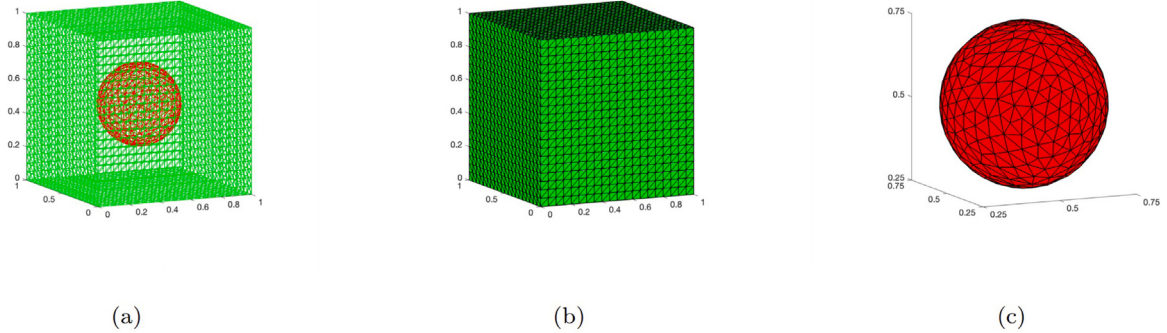


Fig. 3. 3D visualization of a generated RVE with a spherical inclusion: (a) RVE; (b) matrix; (c) spherical inclusion.

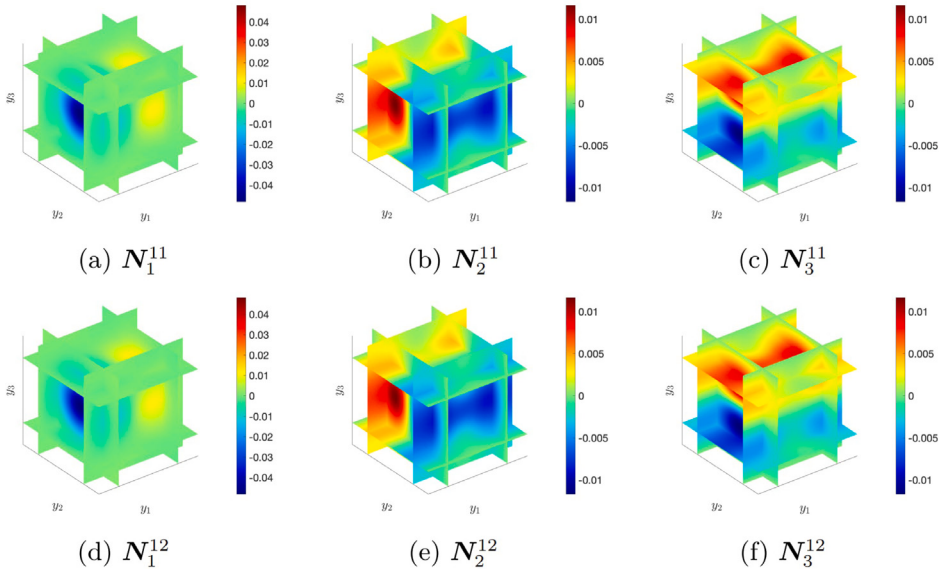


Fig. 4. First-order cell functions $N_1^{11}(y)$ and $N_1^{12}(y)$ when the normalized radius of the spherical inclusion is set as $R = 0.25$.

Fig. 3 shows the mesh configuration of a RVE containing a spherical inclusion. Due to the symmetry of this microstructure, the number of independent vector-valued first-order cell functions is reduced to two, specifically N_1^{11} and N_1^{12} , as derived in Appendix B. The solutions for these cell functions, obtained via finite element simulations, are presented in Fig. 4. These results confirm the theoretical symmetric and anti-symmetric properties of the first-order cell functions, as discussed in Appendix B. In particular, N_1^{11} is anti-symmetric with respect to the plane $y_1 = 0.5$, while N_1^{12} is symmetric about the same plane.

After obtaining the numerical solutions for N^{pq} , the homogenized elasticity tensor C , strain gradient stiffness tensor D , and micro-inertial tensor F are computed using the integral expressions in Eqs. (20), (22) and (26). Fig. 5 illustrates the variation of C , D , and F as functions of the normalized radius for spherical inclusions. The components of the homogenized elasticity tensor C_{ijkl} exhibit a monotonic decrease as the inclusion size increases, transitioning from the elastic modulus of the matrix to that of the inclusion. In contrast, the components of the strain gradient stiffness tensor D_{ijklmn} and micro-inertial tensor F_{ijkl} display non-monotonic relationships with the normalized inclusion radius. As the inclusion radius increases from 0 to approximately 0.5, the values of D_{ijklmn} and F_{ijkl} initially increase, reach a peak, and then decrease. Notably, the peak values of all components occur near a normalized radius of 0.44, though slight variations exist in the exact peak positions.

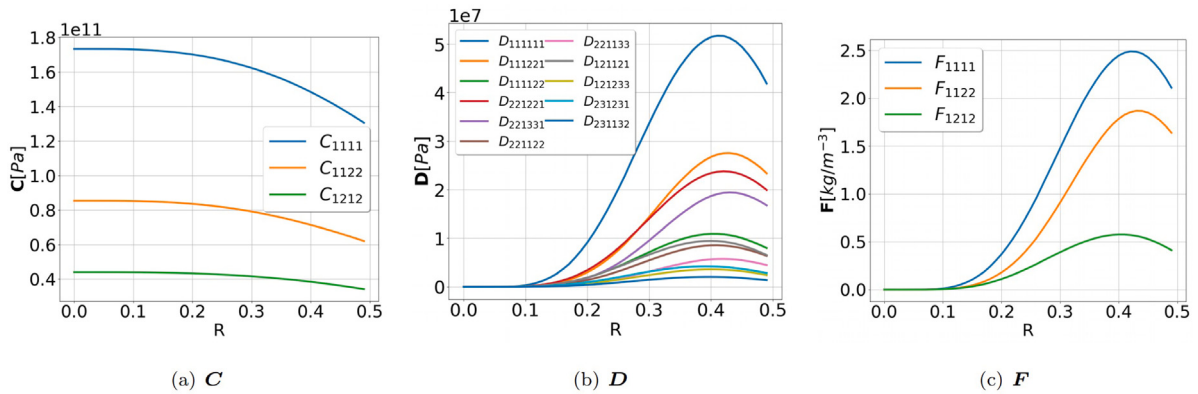


Fig. 5. Variation of CDF with normalized radius R for a spherical inclusion.

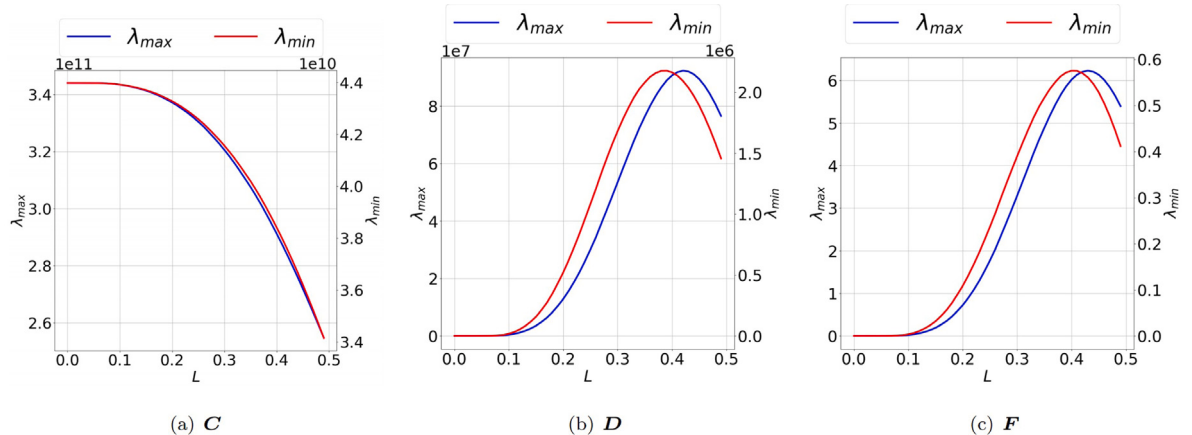


Fig. 6. Variation of minimum and maximum eigenvalues of CDF with normalized radius R for a spherical inclusion.

This non-monotonic behavior highlights the complex interactions between the matrix and inclusion phases, where the degree of material heterogeneity plays a pivotal role. For small inclusions, the material response is matrix-dominated, leading to lower values of \mathbf{D} and \mathbf{F} . As the inclusion radius increases, the material becomes more heterogeneous, with the inclusions exerting a more significant influence on the macroscopic response. This results in an initial rise in \mathbf{D} and \mathbf{F} . Around a normalized radius of 0.44, the contributions of the matrix and inclusion become comparable, maximizing the heterogeneity effects and resulting in peak values of \mathbf{D} and \mathbf{F} . As the inclusion radius continues to grow, the inclusions dominate the material behavior, reducing heterogeneity and causing a decline in \mathbf{D} and \mathbf{F} . This non-monotonic trend reflects a transition from a matrix-dominated state (low heterogeneity) to a matrix-inclusion-dominated state (high heterogeneity) and finally to an inclusion-dominated state (low heterogeneity).

As described in Eq. (27), \mathbf{D} and \mathbf{F} characterize the coupling between strain gradients, strain rates, and the homogenized strain and kinetic energy functions respectively. Their magnitudes quantify the significance of strain gradient and strain rate effects. When \mathbf{D} and \mathbf{F} are zero, strain gradient and strain rate effects vanish, reducing the model to the traditional continuum mechanics framework. Conversely, larger values of \mathbf{D} and \mathbf{F} indicate more pronounced strain gradient and strain rate effects. Fig. 5 thus demonstrates that the importance of strain gradient and strain rate effects in the elastic-dynamic response of composite materials is strongly correlated with the volume fraction of the inclusions.

Fig. 6 illustrates the variation of the minimum and maximum eigenvalues of the tensors \mathbf{C} , \mathbf{D} , and \mathbf{F} (in Voigt matrix form) with respect to the normalized radius of spherical inclusions. The eigenvalues remain strictly positive for all non-homogeneous inclusion cases, thereby confirming the positive definiteness of \mathbf{C} , \mathbf{D} , and \mathbf{F} as outlined in Eqs. (40a)–(40b). Both the minimum and maximum eigenvalues of \mathbf{D} and \mathbf{F} exhibit non-monotonic behavior, consistent with the trends observed in their individual components. Similarly, the other eigenvalues demonstrate comparable variation patterns, as shown in Fig. C.1.

For the case of spherical inclusions, as the normalized inclusion radius reaches its maximum value of 0.5, the material remains a heterogeneous composite, meaning that the tensors \mathbf{D} and \mathbf{F} do not decrease completely to zero. To further demonstrate that \mathbf{D} and \mathbf{F} serve as quantitative measures of heterogeneity, we designed an RVE containing cubic inclusions, as shown in Fig. 7. Fig. 8 illustrates the variation of \mathbf{C} , \mathbf{D} , and \mathbf{F} with respect to the normalized length L . It is evident that as the normalized inclusion length approaches 1, all components of \mathbf{D} and \mathbf{F} decrease to zero. The eigenvalue variation curves presented in Fig. 9 and Fig. C.2 exhibit

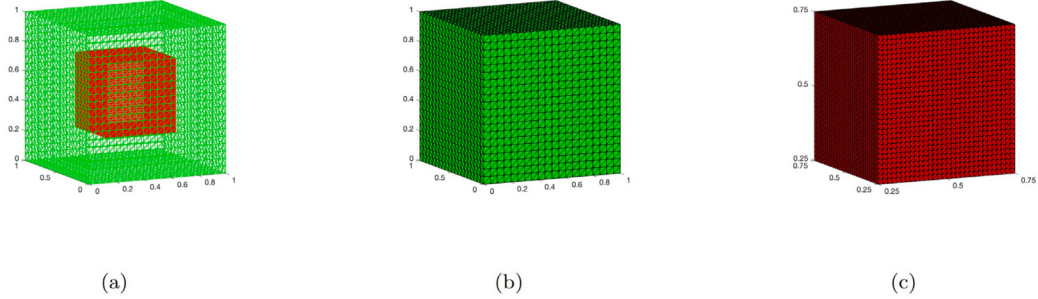


Fig. 7. 3D visualization of a generated RVE with a cubic inclusion: (a) RVE; (b) matrix; (c) cubic inclusion.

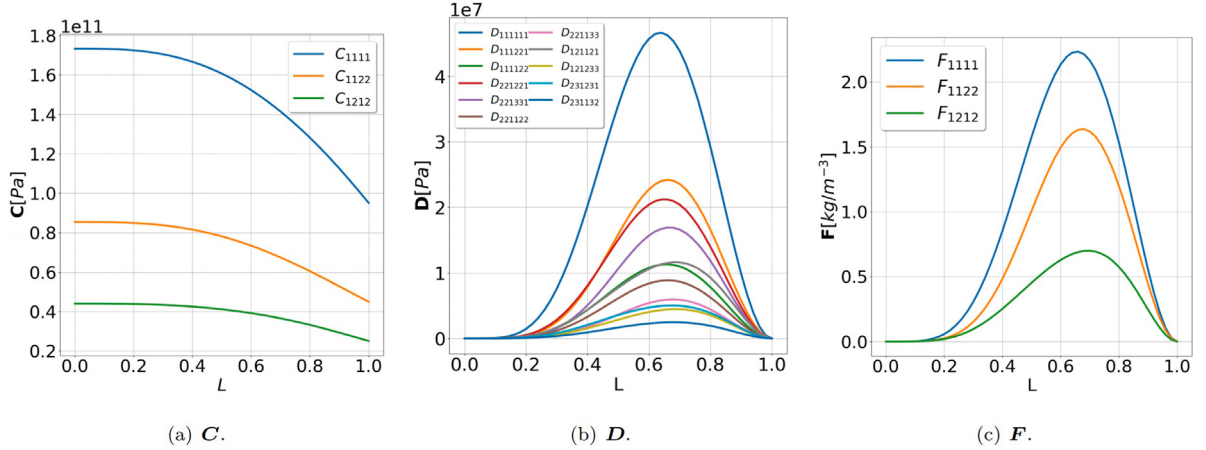


Fig. 8. Variation of CDF with normalized side length L for a cubic inclusion.

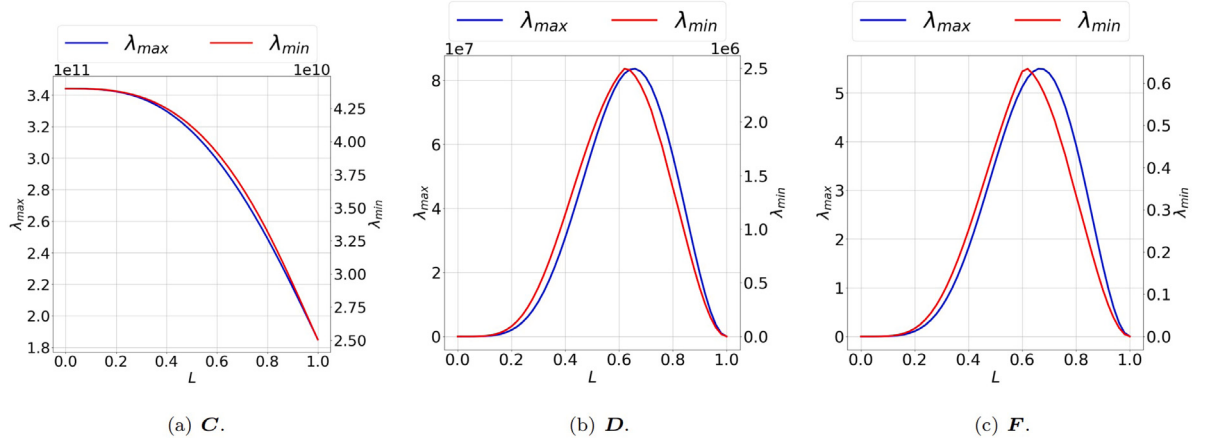


Fig. 9. Variation of minimum and maximum eigenvalue of CDF with normalized side length L for a cubic inclusion.

similar trends. This occurs because, as the normalized length of the inclusion increases from 0 to 1, the material transitions from one homogeneous material (ZrO_2) to another homogeneous material (Ti–C6Al–C4V).

As discussed in Section 2.3, our model can be reduced to Aifantis's two-parameter strain gradient model by minimizing the Frobenius norm of the coefficient tensors between the two models. In other words, the values of $\mathbf{C}, \mathbf{D}, \mathbf{F}$ can be used to calibrate the normalized homogenized internal length L_s and normalized homogenized internal inertia L_d in Aifantis's model. Fig. 10 shows the

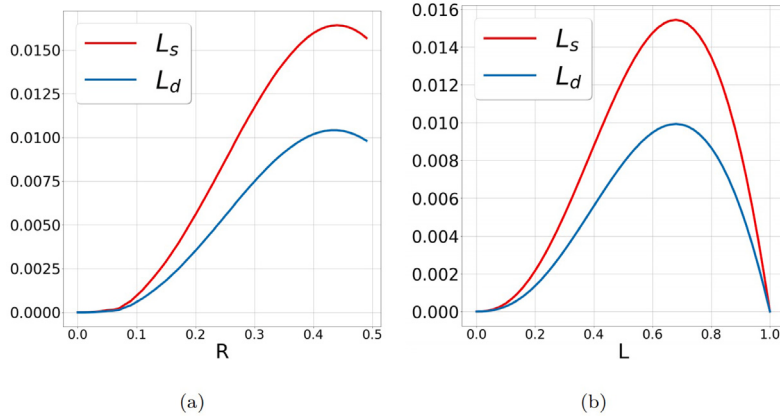


Fig. 10. (a) Variation of L_s and L_d with normalized radius R for a spherical inclusion; (b) Variation of L_s and L_d with normalized side length L for a cubic inclusion.

variation of L_s and L_d calibrated using this method with respect to changes in the microstructural properties. These trends exhibit similar behavior to that of \mathbf{D} and \mathbf{F} , reflecting the interplay between the matrix and inclusions.

4.2. Macro-structure analysis

In this subsection, we apply the developed model to predict the elastodynamic behaviors of macroscopic structures, in comparison with classical homogenized model. To this end, the numerical solutions of the strain gradient elastodynamic equations (Eq. (36a)) are obtained by using the finite element method (FEM) for spatial discretization the Newmark method for temporal discretization [75,76]. Within the finite element framework, the displacement field $\mathbf{u}(t, \mathbf{x})$ is spatially discretized and approximated within each element by a set of shape functions $\Phi_i(\mathbf{x})$, such that $\mathbf{u}(t, \mathbf{x}) = \mathbf{U}_i(t)\Phi_i(\mathbf{x})$, where $\mathbf{U}_i(t)$ denotes the nodal displacements. The governing equation of motion in Eq. (36a) is then discretized, resulting in the following algebraic system:

$$\begin{cases} \mathbf{K}\ddot{\mathbf{U}}(t) + \mathbf{M}\dot{\mathbf{U}}(t) = \mathbf{F}(t), \\ \mathbf{U}(0) = \mathbf{U}_0; \quad \dot{\mathbf{U}}(0) = \mathbf{U}_1, \end{cases} \quad (51)$$

where, the stiffness matrix M_{pq} , the mass matrix K_{pq} , and the external force vector $F_p(t)$ are computed through the following integrals:

$$\begin{aligned} M_{pq} &= \int_{\Omega} \hat{\rho} \Phi_p(\mathbf{x}) \Phi_q(\mathbf{x}) \, d\mathbf{x} + \varepsilon^2 \int_{\Omega} F_{ijkl} e_{ij}(\Phi_p)(\mathbf{x}) e_{kl}(\Phi_q)(\mathbf{x}) \, d\mathbf{x} \\ K_{pq} &= \int_{\Omega} C_{ijkl} e_{ij}(\Phi_p)(\mathbf{x}) e_{kl}(\Phi_q)(\mathbf{x}) \, d\mathbf{x} + \varepsilon^2 \int_{\Omega} D_{ijklmn} e_{ijk}(\Phi_p)(\mathbf{x}) e_{lmn}(\Phi_q)(\mathbf{x}) \, d\mathbf{x}, \\ F_p(t) &= \int_{\Omega} f(t, \mathbf{x}) \Phi_p(\mathbf{x}) \, d\mathbf{x}. \end{aligned}$$

Next, we apply the Newmark method for temporal discretization of Eq. (51). The time domain is divided into small intervals with step Δt , the solution at each time step $t_n = n \times \Delta t$ is denoted as $\mathbf{U}^n = \mathbf{U}(t_n)$ which is updated through Algorithm 1. When $\gamma \geq 0.5$ and $\beta \geq 0.25(0.5 + \gamma)^2$, the Newmark method is unconditionally stable. In this study, the parameters are chosen as $\gamma = 0.5$ and $\beta = 0.25$.

4.2.1. Beam vibration

In this subsection, we investigate the capability of the homogenized strain gradient elastodynamic (HSG) model to approximate the dynamic response of periodic composite materials through simulation of beam vibration. The beam under consideration has geometric dimensions defined by $\Omega = [0, 0.1 \text{ m}] \times [0, 0.1 \text{ m}] \times [0, 1 \text{ m}]$ and contains periodically distributed spherical inclusions. The inclusions are arranged with a periodicity of $\varepsilon = 0.1 \text{ m}$ and have a radius of $r = 0.025 \text{ m}$, corresponding to a normalized radius of $R = r/\varepsilon = 0.25$. The configuration of the composite beam, including the inclusion distribution, is illustrated in Fig. 11(a).

The beam is subjected to a time-dependent body force defined as:

$$\mathbf{f} = \begin{cases} (0, 0, 10^9 t), & 0 \leq t \leq 0.08 \text{ s}, \\ (0, 0, 0), & t > 0.08 \text{ s}. \end{cases} \quad (52)$$

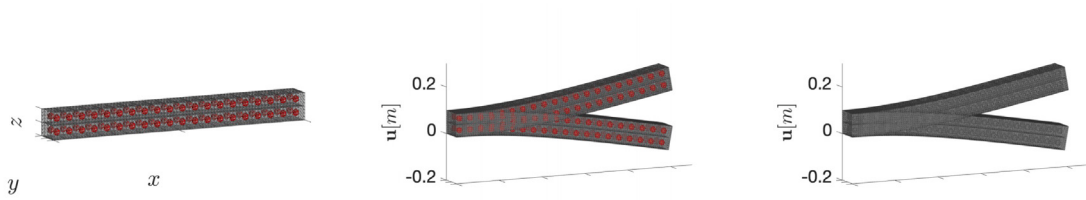
Homogeneous Dirichlet boundary condition is imposed on the left boundary, ensuring that $\mathbf{u}(x, y, z) = (0, 0, 0)$ for $x = 0$.

Algorithm 1: Newmark

```

Result:  $\mathbf{U}^N$ ;
Data:  $\mathbf{U}^0, \dot{\mathbf{U}}^0$ ;
1  $n = 1$ ;
2 while  $n \leq N$  do
3    $\mathbf{K}_{\text{eff}} = \mathbf{K} + \frac{1}{\beta \Delta t^2} \mathbf{M}$ ;
4    $\mathbf{F}_{\text{eff}} = \mathbf{F}(t_n) + \mathbf{M} \left( \frac{1}{\beta \Delta t^2} \mathbf{U}^{n-1} + \frac{1}{\beta \Delta t} \dot{\mathbf{U}}^{n-1} + \left( \frac{1}{2\beta} - 1 \right) \ddot{\mathbf{U}}^{n-1} \right)$ ;
5    $\mathbf{U}^n = \mathbf{K}_{\text{eff}}^{-1} \mathbf{F}_{\text{eff}}$ ;
6    $\dot{\mathbf{U}}^n = \frac{1}{\beta \Delta t^2} \left( \mathbf{U}^n - \mathbf{U}^{n-1} - \Delta t \dot{\mathbf{U}}^{n-1} - \left( \frac{1}{2} - \beta \right) \Delta t^2 \ddot{\mathbf{U}}^{n-1} \right)$ ;
7    $\ddot{\mathbf{U}}^n = \dot{\mathbf{U}}^{n-1} + (1 - \gamma) \Delta t \dot{\mathbf{U}}^{n-1} + \gamma \Delta t \ddot{\mathbf{U}}^n$ ;
8    $n = n + 1$ ;
9 end

```



(a) Structure of beam with spherical inclusions. (b) RS at $t = 0.081\text{s}$ (top) and $t = 0.0875\text{s}$ (bottom). (c) HSG at $t = 0.081\text{s}$ (top) and $t = 0.0875\text{s}$ (bottom).

Fig. 11. Deformation of beam with spherical inclusions of $r = 0.025\text{ m}$ and $\epsilon = 0.1\text{ m}$.

The direct numerical simulation (DNS) solution based on a tetrahedral mesh that explicitly resolves the inclusions is used as the reference solution (RS). This solution is computed using a tetrahedral mesh that explicitly resolves the inclusions. Numerical results for $t = 0.081\text{s}$ (top) and $t = 0.0875\text{s}$ (bottom) are presented in Fig. 11(b), while corresponding outcomes from the homogenized strain gradient (HSG) model are depicted in Fig. 11(c). A detailed comparison of strain energy over time between the homogenized strain gradient solutions and the reference solutions is provided in Fig. 12(a). Additionally, Fig. 12(b) illustrates the z -direction displacement at the material point $(1\text{ m}, 0.05\text{ m}, 0)$.

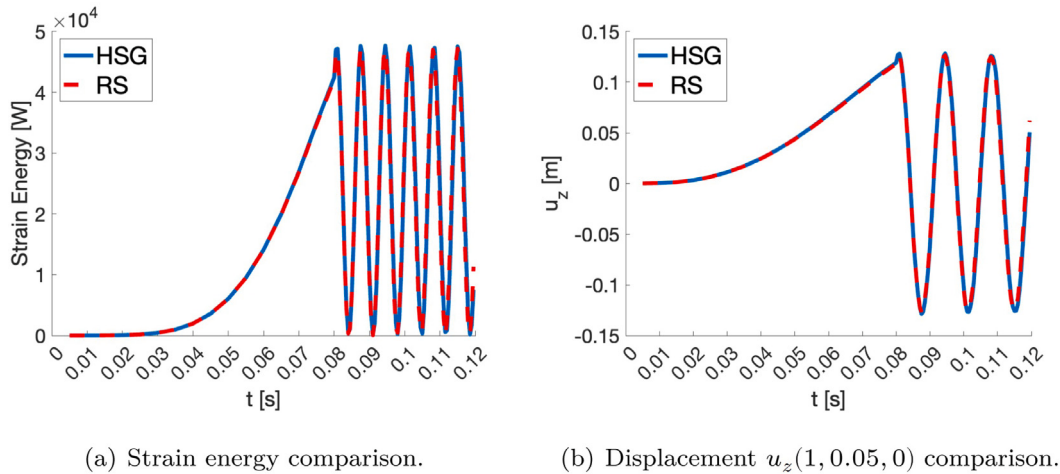
The global displacement field, strain energy distribution, and the temporal variation of displacement at specific points show excellent agreement between the homogenized strain gradient solution and the reference solution. This underscores the capability of the homogenized strain gradient elastodynamics model to predict the dynamic mechanical response of periodic composite materials with high fidelity. Moreover, as the homogenized solution does not necessitate resolving the explicit distribution of inclusions, it permits the use of a uniform coarse mesh. This approach serves as a computationally efficient alternative to the high-resolution reference solution, significantly reducing computational complexity while maintaining accuracy, making it a practical choice for real-world applications.

4.2.2. L-shaped structural analysis

To advance the study, we aim to examine the mitigation or smoothing of singularities in static problems, which are commonly observed at non-convex corners or at the points of application of concentrated loads in classical elasticity [13,77]. Our investigation will focus on comparing the solutions obtained using static homogenized strain gradient equations (HSG, Eq. (37)) with those derived from classical homogenized elasticity equations (HE, neglecting the ϵ -dependent term in Eq. (37)). For this purpose, we consider a three-dimensional L-shaped structure comprising three $1\text{ m} \times 1\text{ m} \times 1\text{ m}$ cubes featuring spherical inclusions, as illustrated in Fig. 13(a). The boundary conditions are imposed on the faces highlighted in red as follows:

$$\frac{\partial u}{\partial n} = 0, \quad v = -0.1(2 - y), \quad w = -0.1(2 - z). \quad (53)$$

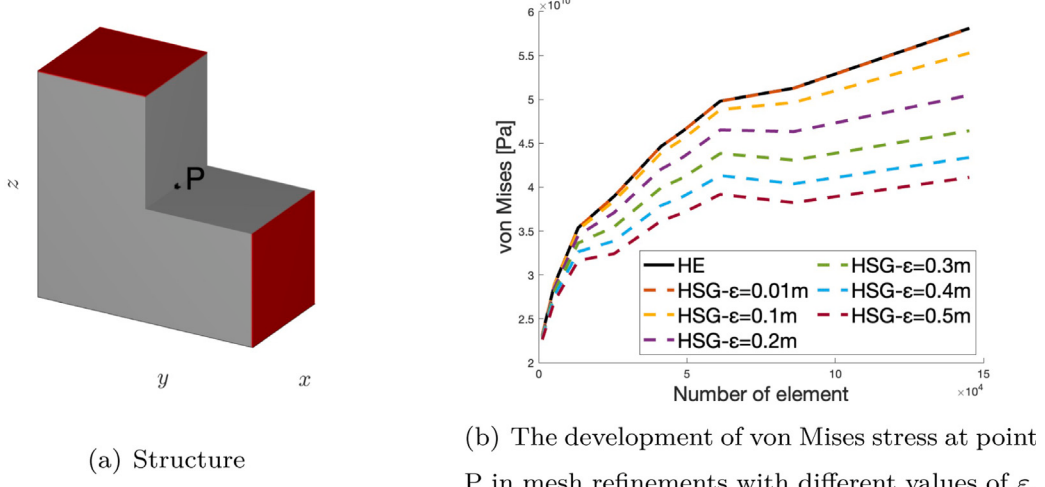
Fig. 13(b) illustrates the variation of von Mises stress at the center of the non-convex corner (point P in Fig. 13(a)) as the mesh is progressively refined, for a normalized inclusion radius of 0.44. The analysis indicates a significant reduction in stress singularity at the non-convex region as ϵ increases. Specifically, when the RVE size is $\epsilon = 0.01\text{ m}$, the results computed by the strain gradient model are nearly indistinguishable from those of the homogenized elasticity model. However, when $\epsilon = 0.5\text{ m}$, with the RVE size comparable to that of the macroscopic L-shaped structure, the singularity predicted by the strain gradient model is approximately half of that obtained from the homogenized elasticity model, except in cases with excessively coarse meshes.



(a) Strain energy comparison.

(b) Displacement $u_z(1, 0.05, 0)$ comparison.

Fig. 12. Comparison of strain energy and displacement variations with time between HSG and RS.



(a) Structure

(b) The development of von Mises stress at point P in mesh refinements with different values of ϵ .

Fig. 13. L-shaped structural analysis.

It is also widely recognized that incorporating strain gradient effects can reduce the mesh-dependence of simulation results [4,35]. As observed in Fig. 13(b), the stress predicted by the homogenized elasticity model exhibits a significant dependence on mesh refinement, with the stress values increasing as the number of elements is enhanced. In contrast, for solutions derived from the homogenized strain gradient equations, when ϵ reaches 0.5 m, the von Mises stress stabilizes and converges to a bounded value, indicating reduced mesh sensitivity. To further explore this, we compare the von Mises stress distributions for a fixed normalized inclusion radius $R = 0.44$, $\epsilon = 0.5$ m, and different mesh discretizations of 113,379, 145,227, and 181,992 elements, as shown in Fig. 14. As observed, the use of the homogenized strain gradient model results in minimal changes in the stress field with increasing mesh refinement in the non-convex region. This behavior highlights the low degree of mesh sensitivity in the strain gradient solutions.

4.2.3. Plane-impacting analysis

In this subsection, we investigate the mitigation of stress singularities arising during impact experiments. The target is modeled as a cylindrical body with a cone-shaped recess at the upper end, characterized by a radius of 0.01 m and a height of 0.016 m, containing spherical inclusions with a normalized radius $R = 0.44$. The overall height of the recess measures 0.08 m, as depicted in Fig. 15(a). A flyer impacts the lower end of the target at a velocity of 400 m s^{-1} , generating shock compression waves that propagate through both the flyer and the target. Upon reaching the recess, the shock wave induces stress singularities in the two non-convex regions: at the apex of the recess and along the upper edge.

Fig. 15(b) presents the temporal evolution of von Mises stress at the apex of the recess. The results clearly demonstrate that, when employing the homogenized strain gradient (HSG) elastodynamics equations, the computed stress levels are generally lower compared to those obtained using the classical homogenized elasticity (HE) equations. This difference becomes pronounced as the

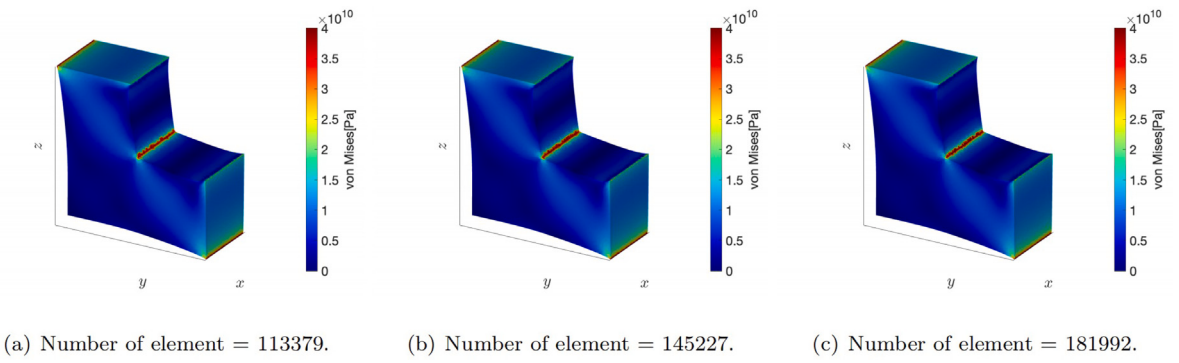
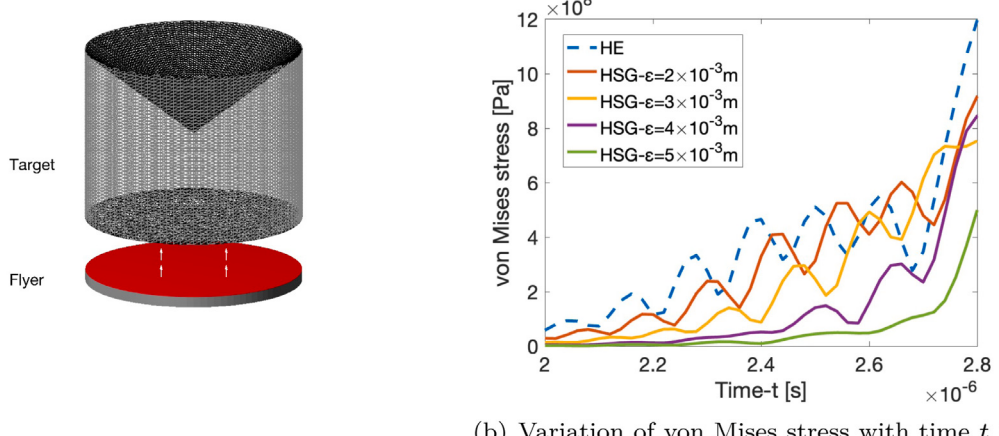


Fig. 14. 3D visualization of von Mises stress with different meshes.



(a) Structure of the target and flyer.

(b) Variation of von Mises stress with time t for different ε .

Fig. 15. Plane-impacting analysis.

parameter ε increases. Notably, when ε approaches the characteristic length scale of the material, particularly at $\varepsilon = 5 \times 10^{-3} \text{ m}$, the stress singularity is substantially mitigated. Fig. 16 provides a more intuitive depiction of the von Mises stress distribution at $t = 2.4 \times 10^{-6} \text{ s}$. It is evident that, in the two non-convex regions, the stress levels predicted by the strain gradient model are significantly lower than those predicted by the classical linear elasticity model. This observation highlights the effectiveness of the strain gradient model in alleviating stress concentrations, particularly in regions characterized by sharp geometric features.

4.2.4. Wave dispersion

Another motivation for employing strain gradient elastodynamics is its capability to accurately describe dispersive wave propagation in heterogeneous media [69,78,79]. In the case of a material containing periodically arranged spherical inclusions, we investigate the effects of the inclusion average spacing ε and the normalized radius R on the dispersion relation.

Consider a longitudinal wave propagating in the x_1 -direction, denoted as $u_1(x_1, t)$. According to Eq. (36a), u_1 satisfies the following partial differential equation (PDE):

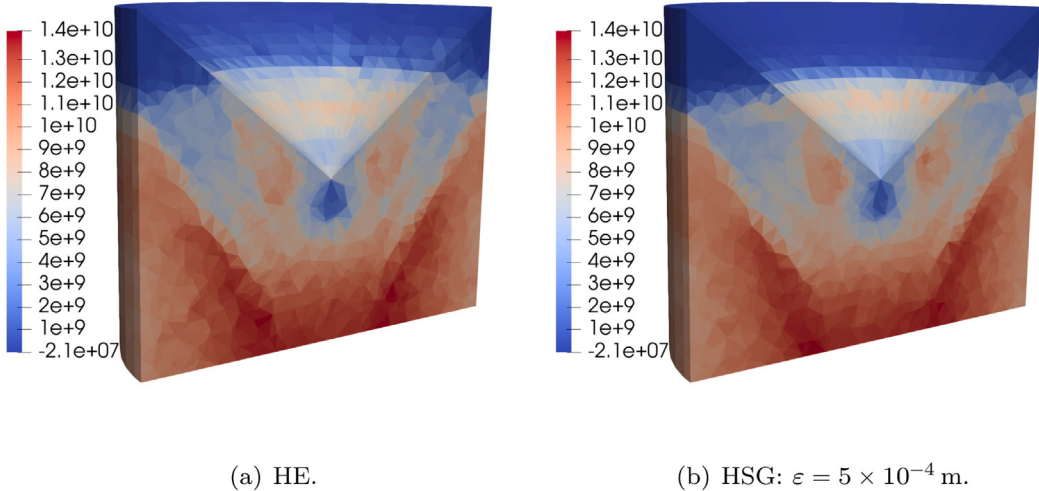
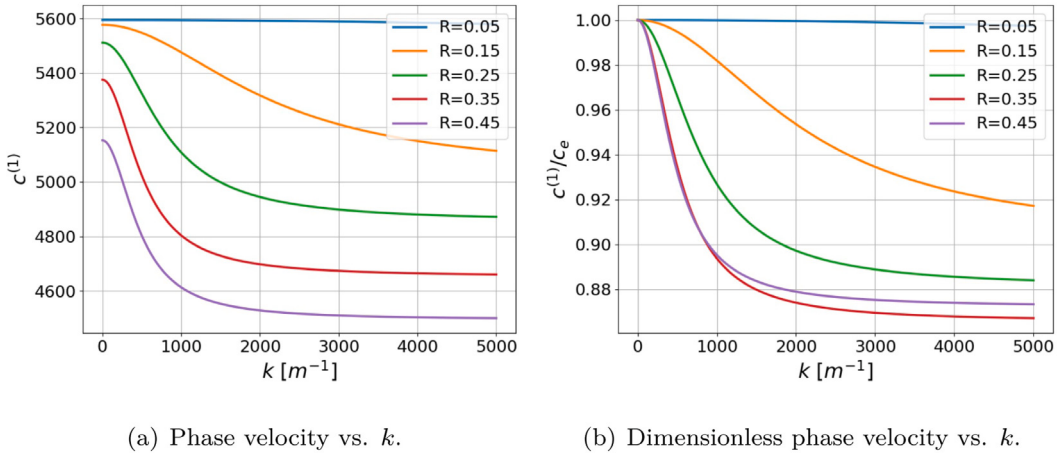
$$C_{1111} \frac{\partial^2 u_1}{\partial x_1 \partial x_1} - \varepsilon^2 D_{111111} \frac{\partial^4 u_1}{\partial x_1 \partial x_1 \partial x_1 \partial x_1} = \hat{\rho} \ddot{u}_1 - \varepsilon^2 F_{1111} \frac{\partial^2 \ddot{u}_1}{\partial x_1 \partial x_1}. \quad (54)$$

To derive the dispersion relation, we assume harmonic wave solutions of the form:

$$u_1(x_1, t) = \hat{u}_1 e^{i(kx_1 - \omega t)}, \quad (55)$$

where k is the wavenumber, ω is the frequency, and i is the imaginary unit ($i^2 = -1$). Substituting Eq. (55) into Eq. (54) yields the following dispersion relation for the phase velocity:

$$c^{(1)} = \frac{\omega}{k} = \sqrt{\frac{C_{1111} + k^2 \varepsilon^2 D_{111111}}{\hat{\rho} + k^2 \varepsilon^2 F_{1111}}} = c_e \sqrt{\frac{1 + k^2 \varepsilon^2 D_{111111}/C_{1111}}{1 + k^2 \varepsilon^2 F_{1111}/\hat{\rho}}}, \quad (56)$$

Fig. 16. 3D visualization of von Mises stress at $t = 2.4 \times 10^{-6}$ s.Fig. 17. Wave dispersion curve with $\epsilon = 0.1$ m.

where $c_e = \sqrt{C_{1111}/\hat{\rho}}$ represents the phase velocity derived from the classical homogenization method, which remains constant. As can be observed, when $k \rightarrow 0$, the phase velocity $c^{(1)}$ approaches the classical homogenized phase velocity c_e . On the other hand, as $k \rightarrow \infty$, the phase velocity $c^{(1)}$ approaches a finite bound given by

$$c_e \sqrt{\frac{D_{111111}/C_{1111}}{F_{1111}/\hat{\rho}}}.$$

Neglecting the micro-inertia term in Eq. (54) results in an unphysical infinite phase velocity as $k \rightarrow \infty$. Therefore, the strain gradient stiffness tensor \mathbf{D} alone is insufficient to produce realistic dispersion curves, highlighting the necessity of incorporating the micro-inertia tensor \mathbf{F} .

Fig. 17(a) shows the influence of the normalized inclusion radius R on the dispersion relation while keeping $\epsilon = 0.1$ m constant. For a fixed wavenumber, increasing R results in a lower phase velocity. In contrast, Fig. 17(a) shows the dimensionless dispersion curves, clearly demonstrating that stronger material heterogeneity results in more pronounced dispersion effects. When R takes values from the set $\{0.05, 0.15, 0.25, 0.35\}$, the increasing radius intensifies the heterogeneity, leading to stronger dispersion. Specifically, as the wavenumber increases, the wave speed deviates more rapidly from the classical homogenized phase velocity $c_e^{(1)}$ when $R = 0.45$, the degree of material heterogeneity decreases compare to $R = 0.35$, which in turn reduces the dispersion effect.

Fig. 18 illustrates the effect of ϵ on the dispersion relation for a fixed $R = 0.35$. In this case, the normalized radius of the material remains the same, so the classical phase velocity $c_e^{(1)}$ is identical. The variation in ϵ can be interpreted as a scaling transformation of the entire material structure. According to Eq. (56), ϵ does not affect the asymptotic wave speed, and the relationship between

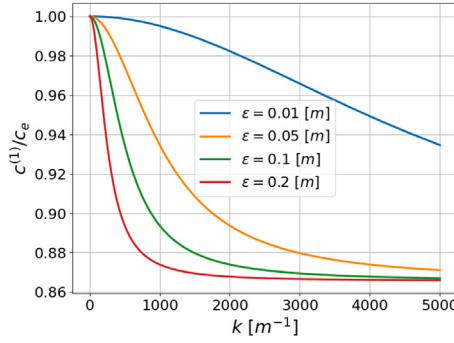


Fig. 18. Dimensionless phase velocity vs. k with fixed $R = 0.35$.

the phase velocity and the dimensionless wavenumber εk . However, as ε increases, the degree of dispersion becomes higher, and the asymptotic phase velocity is reached more rapidly.

5. Discussion: comparisons to higher order models

In this section, we investigate the higher-order homogenized strain energy and kinetic energy, along with the corresponding elastodynamic equations. We explore the impact of higher-order truncation of the displacement \mathbf{u}^ε on both strain energy and kinetic energy, and analyze the advantages of adopting the first-order truncated strain gradient elastodynamic equation (Eq. (36a)), particularly in terms of its accuracy and computational complexity.

According to asymptotic homogenization theory, the formal asymptotic expansion of the displacement field \mathbf{u}^ε (Eq. (4)) takes the following double-series structure, as presented in Chapter 4, Section 5 of Bakhvalov and Panasenko [65] and rigorously discussed in [50]:

$$\mathbf{u}^\varepsilon(\mathbf{x}, t) = \mathbf{v}(\mathbf{x}, t) + \sum_{n=1}^{\infty} \varepsilon^n \mathbf{v}^{(n)}(\mathbf{x}, t) = \mathbf{v}(\mathbf{x}, t) + \sum_{n=1}^{\infty} \varepsilon^n \mathbf{N}^{[n]}(\frac{\mathbf{x}}{\varepsilon}) e_{x[n]}(\mathbf{v}(\mathbf{x}, t)). \quad (57)$$

Here, $\mathbf{v}(\mathbf{x}, t) = \sum_{n=0}^{\infty} \varepsilon^n \mathbf{v}_n(\mathbf{x}, t)$. The explicit form of $\mathbf{v}_n(\mathbf{x}, t)$ can be found in Chapter 4, Section 5 of Bakhvalov and Panasenko [65], but it is not essential in this study, as we treat $\mathbf{v}(\mathbf{x}, t)$ as the macroscopic homogenized displacement field to derive the governing equation it satisfies. This approach is analogous to the role of $\mathbf{u}^{(0)}$ discussed earlier. The multi-index $[n]$ is defined as $[n] = m_1 \dots m_{n+1}$ for $n \geq 1$. The notation $e_{x[n]}(\mathbf{v})$ represents the strain field and its higher-order spatial derivatives with respect to the macroscopic variable \mathbf{x} and is defined as

$$e_{x[n]}(\mathbf{v}) = \begin{cases} e_{xm_1 m_2}(\mathbf{v}) = \frac{1}{2} \left(\frac{\partial v_{m_1}}{\partial x_{m_2}} + \frac{\partial v_{m_2}}{\partial x_{m_1}} \right), & n = 1, \\ e_{xm_1 \dots m_{n+1}}(\mathbf{v}) = \frac{\partial^{n-1} e_{xm_1 m_2}(\mathbf{v})}{\partial x_{m_3} \dots \partial x_{m_{n+1}}}, & n \geq 2. \end{cases} \quad (58)$$

Similarly, the corresponding notations $e_{y[n]}(\mathbf{u})$ with respect to the microscopic variable \mathbf{y} are defined analogously. The vector-valued function $\mathbf{N}^{[n]} \in \mathcal{D}(Y)$ is called the n th order cell function. In particular, the first-order cell function, $\mathbf{N}^{[1]}$, is defined in Eq. (9), and the second-order cell function is given by

$$\frac{\partial}{\partial y_j} a_{ijkl} e_{ykl}(\mathbf{N}^{m_1 m_2 m_3}) + \frac{\partial}{\partial y_j} a_{ijkm_3} \mathbf{N}_k^{m_1 m_2} + a_{im_3 kl} e_{ykl}(\mathbf{N}^{m_1 m_2}) + a_{im_3 m_1 m_2} = C_{im_3 m_1 m_2}. \quad (59)$$

For higher-order cell functions $\mathbf{N}^{[n]}$ with $n \geq 3$, the governing equation can be expressed as

$$\frac{\partial}{\partial y_j} a_{ijkl} e_{ykl}(\mathbf{N}^{[n-2]m_n m_{n+1}}) + \frac{\partial}{\partial y_j} a_{ijkm_{n+1}} \mathbf{N}_k^{[n-2]m_n} + a_{im_{n+1} kl} e_{ykl}(\mathbf{N}^{[n-2]m_n}) + a_{im_{n+1} km_n} \mathbf{N}_k^{[n-2]} = 0. \quad (60)$$

If the displacement field in Eq. (57) is retained without truncation, the higher-order homogenized strain energy can be expressed as

$$\begin{aligned} W &= \frac{1}{|Y_\varepsilon|} \int_{Y_\varepsilon} \frac{1}{2} a_{ijkl} e_{ij}(\mathbf{u}^\varepsilon) e_{kl}(\mathbf{u}^\varepsilon) d\mathbf{x} \\ &= \frac{1}{|Y_\varepsilon|} \int_{Y_\varepsilon} \frac{1}{2} a_{ijkl} \left[e_{xij}(\mathbf{v}^{(0)}) + \sum_{p \geq 1} (\varepsilon^p e_{xij}(\mathbf{v}^{(p)}) + \varepsilon^{p-1} e_{yij}(\mathbf{v}^{(p)})) \right] \left[e_{xkl}(\mathbf{v}^{(0)}) + \sum_{q \geq 1} (\varepsilon^q e_{xkl}(\mathbf{v}^{(q)}) + \varepsilon^{q-1} e_{ykl}(\mathbf{v}^{(q)})) \right] d\mathbf{x} \\ &= \frac{1}{2} \hat{C}_{ijkl} \mathcal{E}_{ij} \mathcal{E}_{kl} + \sum_p \varepsilon^p \hat{G}_{ij[p]l} \mathcal{E}_{ij} \mathcal{E}_{[p]l} + \sum_{pq \geq 1} \frac{\varepsilon^{p+q}}{2} \hat{D}_{[p]j[q]l} \mathcal{E}_{[p]j} \mathcal{E}_{[q]l} + \sum_{p \geq 2, q \geq 1} \varepsilon^{p+q-1} \hat{I}_{[p][q]l} \mathcal{E}_{[p]} \mathcal{E}_{[q]l} + \sum_{pq \geq 2} \frac{\varepsilon^{p+q-2}}{2} \hat{S}_{[p][q]} \mathcal{E}_{[p]} \mathcal{E}_{[q]}, \end{aligned} \quad (61)$$

and the homogenized kinetic energy density is given by

$$\begin{aligned} K &= \frac{1}{|Y_\epsilon|} \int_{Y_\epsilon} \frac{\rho}{2} \dot{v}_i^\epsilon \dot{v}_i^\epsilon d\mathbf{x} = \frac{1}{|Y_\epsilon|} \sum_{pq \geq 0} \int_{Y_\epsilon} \frac{\rho}{2} \epsilon^{p+q} \dot{v}_i^{(p)} \dot{v}_i^{(q)} d\mathbf{x} \\ &= \frac{\hat{\rho}}{2} \dot{v}_i \dot{v}_i + \sum_{p \geq 1} \epsilon^p \hat{H}_{i[p]} \dot{v}_i \mathcal{E}_{[p]} + \sum_{pq \geq 1} \frac{\epsilon^{p+q}}{2} \hat{F}_{[p][q]} \dot{\mathcal{E}}_{[p]} \dot{\mathcal{E}}_{[q]}. \end{aligned} \quad (62)$$

In Eqs. (61) and (62), $\mathcal{E}_{[p]}$ and $\dot{\mathcal{E}}_{[p]}$ represent the $(p-1)$ th strain gradient and the $(p-1)$ th strain rate of macroscopic displacement \mathbf{v} , respectively. The homogenized moduli are defined as follows:

$$\begin{cases} \hat{C}_{ijkl} = C_{ijkl}, & \hat{G}_{ij[p]l} = \int_Y (a_{ijkl} + a_{mnkl} e_{ymn}(\mathbf{N}^{ij})) N_k^{[p]} dy, \\ \hat{D}_{[p][q]l} = \int_Y a_{ijkl} N_i^{[p]} N_k^{[q]} dy, & \hat{f}_{[p][q]l} = \int_Y a_{ijkl} e_{yij}(\mathbf{N}^{[p]}) N_k^{[q]} dy, \\ \hat{S}_{[p][q]} = \int_Y a_{ijkl} e_{yij}(\mathbf{N}^{[p]}) e_{ykl}(\mathbf{N}^{[q]}) dy, & \\ \hat{H}_{i[p]} = \int_Y \rho N_i^{[p]} dy, & \hat{F}_{[p][q]} = \int_Y \rho N_i^{[p]} N_i^{[q]} dy. \end{cases} \quad (63)$$

For centrosymmetric inclusions, it can be proven that $\hat{\mathbf{G}} = \mathbf{0}$, $\hat{\mathbf{I}} = \mathbf{0}$, and $\hat{\mathbf{H}} = \mathbf{0}$. Moreover, when $p, q = 1$, it follows that $\hat{\mathbf{G}} = \mathbf{G}$, $\hat{\mathbf{D}} = \mathbf{D}$, and $\hat{\mathbf{H}} = \mathbf{H}$. In other words, when $p, q \leq 1$, Eqs. (61) and (62) respectively reduce to Eqs. (27) and (28).

According to Eqs. (61) and (62), a higher-order truncation of the displacement field \mathbf{u}^ϵ introduces the effects of higher-order strain gradients and higher-order strain rates in the strain energy and kinetic energy, respectively. For instance, when the truncation is limited to the second order ($p, q \leq 2$), the homogenized strain energy and kinetic energy will incorporate the second-order strain gradient and strain gradient rate. The explicit expressions are given as

$$\begin{aligned} W &= \frac{1}{2} C_{ijkl} \mathcal{E}_{ij} \mathcal{E}_{kl} + \frac{\epsilon^2}{2} D_{ijklmn} \mathcal{E}_{ijk} \mathcal{E}_{lmn} + \frac{\epsilon^2}{2} S_{ijklmn} \mathcal{E}_{ijk} \mathcal{E}_{lmn} \\ &\quad + \epsilon^3 D_{ijklmno}^1 \mathcal{E}_{ijk} \mathcal{E}_{lmno} + \frac{\epsilon^2}{2} D_{ijklmno}^2 \mathcal{E}_{ijk} \mathcal{E}_{mnop}, \\ K &= \frac{\hat{\rho}}{2} \ddot{u}_i \dot{u}_i + \frac{\epsilon^2}{2} F_{ijkl} \dot{\mathcal{E}}_{ij} \dot{\mathcal{E}}_{kl} + \epsilon^3 F_{ijklm}^1 \dot{\mathcal{E}}_{ij} \dot{\mathcal{E}}_{klm} + \frac{\epsilon^4}{2} F_{ijklmn}^2 \dot{\mathcal{E}}_{ijk} \dot{\mathcal{E}}_{lmn}. \end{aligned} \quad (64)$$

Here, the homogenized moduli \mathbf{S} , \mathbf{D}^1 , \mathbf{D}^2 , \mathbf{F}^1 , and \mathbf{F}^2 are associated with the first- and second-order cell functions and their definitions are expressed as

$$\begin{cases} S_{ijklmn} = \int_Y a_{pqrs} e_{ypq}(\mathbf{N}^{ijk}) e_{yrs}(\mathbf{N}^{lmn}) dy, \\ D_{ijklmno}^1 = \int_Y a_{rks} N_r^{ij} N_s^{lmn} dy, & D_{ijklmno}^2 = \int_Y a_{rls} N_r^{ijk} N_s^{mno} dy, \\ F_{ijklm}^1 = \int_Y \rho N_r^{ijk} N_r^{lm} dy, & F_{ijklmn}^2 = \int_Y \rho N_r^{ijk} N_r^{lmn} dy. \end{cases} \quad (65)$$

By applying the variational principle (Eq. (30)), we obtain the second-order truncated elastodynamic equations as follows:

$$\begin{aligned} \hat{\rho} \ddot{u}_i - \frac{\partial}{\partial x_j} \left(\epsilon^2 F_{ijkl} \dot{\mathcal{E}}_{kl} + \epsilon^3 F_{ijklm}^1 \ddot{\mathcal{E}}_{klm} \right) + \frac{\partial^2}{\partial x_j \partial x_k} \left(\epsilon^3 F_{lmijk}^1 \ddot{\mathcal{E}}_{lm} + \epsilon^4 F_{ijklmn}^2 \ddot{\mathcal{E}}_{lmn} \right) \\ - \frac{\partial}{\partial x_j} \left(C_{ijkl} \mathcal{E}_{kl} \right) + \frac{\partial^2}{\partial x_j \partial x_k} \left(\epsilon^2 (D_{ijklmn} + S_{ijklmn}) \mathcal{E}_{lmn} + \epsilon^3 D_{ijklmno}^1 \mathcal{E}_{lmno} \right) \\ - \frac{\partial^3}{\partial x_j \partial x_k \partial x_l} \left(\epsilon^3 D_{mnijkl}^1 \mathcal{E}_{mno} + \epsilon^4 D_{ijklmno}^2 \mathcal{E}_{mnop} \right) = f_i. \end{aligned} \quad (66)$$

Assuming that the second-order cell functions \mathbf{N}^{pqr} are linearly independent—i.e., for any nonzero $\eta \in \text{sym}(\mathcal{R}^{3 \times 3 \times 3})$, $\eta_{pqr} \mathbf{N}^{pqr} \neq \mathbf{0}$ —it can be shown that the homogenized moduli \mathbf{S} , \mathbf{D}^2 , and \mathbf{F}^2 are symmetric positive definite. Consequently, if the antisymmetric terms in Eq. (66) (which are associated with \mathbf{D}^1 and \mathbf{F}^1) are neglected, the resulting equation (Eq. (66)) is well-posed. The proof is similar to that provided in Appendix D regarding the well-posedness of Eq. (36a).

As in Section 4.2.4, when the second-order truncated elastodynamic equations (Eq. (66)) are applied, the following dispersion relation for a one-dimensional longitudinal wave $u_1(x_1, t) = \hat{u}_1 e^{i(kx_1 - \omega t)}$, is obtained:

$$\begin{aligned} c^{(2)} = \frac{\omega}{k} &= \sqrt{\frac{C_{1111} + k^2 \epsilon^2 D_{111111} + k^2 \epsilon^2 S_{111111} + \epsilon^4 D_{11111111}^2}{\hat{\rho} + k^2 \epsilon^2 F_{1111} + k^4 \epsilon^4 F_{111111}^2}} \\ &= c_e \sqrt{\frac{1 + k^2 \epsilon^2 (D_{111111} + S_{111111}) / C_{1111} + k^4 \epsilon^4 D_{11111111}^2 / C_{1111}}{1 + k^2 \epsilon^2 F_{1111} / \hat{\rho} + k^4 \epsilon^4 F_{111111}^2 / \hat{\rho}}}. \end{aligned} \quad (67)$$

Fig. 19 illustrates the variation of dimensionless phase velocity derived from the elastodynamic equations using first-order and second-order truncations of \mathbf{u}^ϵ , with a fixed value of $\epsilon = 0.1$ m. The results demonstrate that the dispersion relations obtained from

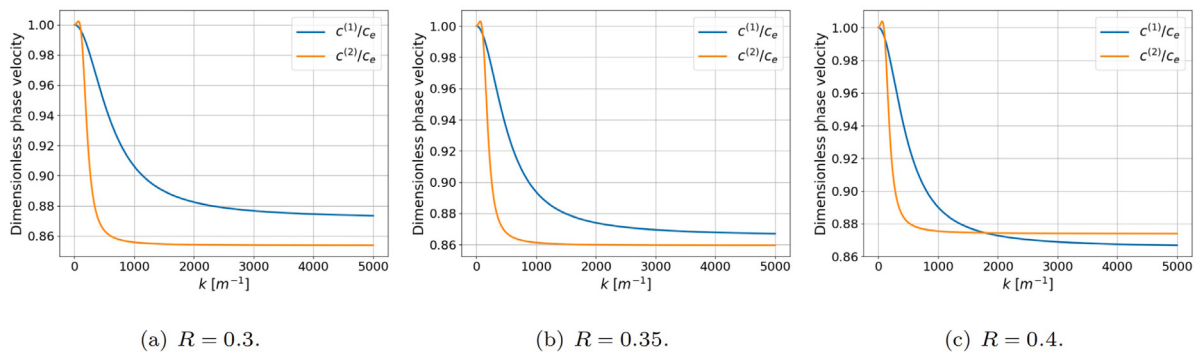


Fig. 19. Comparison of wave dispersion curves obtained from first-order and second-order truncated elastodynamic equations with $\varepsilon = 0.1$ m.

both truncation orders exhibit a high degree of consistency in terms of trend and show only minor quantitative differences, thereby justifying the adoption of the first-order truncation in the present study.

The vector-valued second-order unit cell function consists of 27 components, leading to a significant increase in computational cost. More importantly, the resulting elastodynamic equations take the form of a sixth-order partial differential equation, further intensifying the computational complexity. These equations inherently involve higher-order gradients of strain and strain rate, which, when negligible, render the increased computational effort unnecessary. Furthermore, as established in our previous studies [55,56], employing the first-order truncation to derive the strain and kinetic energies—combined with the application of the Griffith fracture criterion for simulating brittle fracture processes—has yielded results that closely align with experimental observations.

6. Conclusion

In this work, we propose a strain gradient elastodynamics model derived by a variational-asymptotic approach and establish its well-posedness. By employing first-order asymptotic homogenization techniques, we construct homogenized strain and kinetic energy density functions. Subsequently, we derive the governing equations of strain gradient elastodynamics through Hamilton's principle. A key advantage of this methodology is its explicit link between the homogenized coefficients (homogenized elasticity tensor C , strain gradient stiffness tensor D , micro-inertial? tensor F) and the underlying microstructure through time-independent first-order cell functions. Moreover, our model can be simplified to Aifantis' two-parameter strain gradient elastodynamics model by minimizing the Frobenius norm between the coefficient tensors of the two models.

We demonstrate that for arbitrary microstructures, the material parameters \mathbf{C} , \mathbf{D} , and \mathbf{F} , obtained through the proposed two-scale variational-asymptotic method, are symmetric and positive definite. Furthermore, we prove the well-posedness of the strain gradient elastodynamic model, ensuring the existence and uniqueness of solutions, under the conditions of symmetry and positive definiteness of \mathbf{C} , \mathbf{D} , and \mathbf{F} . This result is not specific to our model but applies to general strain gradient elastodynamic frameworks.

Cell analyses reveal that \mathbf{D} and \mathbf{F} are effective quantitative measures of material heterogeneity. For heterogeneous materials, the components and eigenvalues of these tensors exhibit non-monotonic behavior, increasing to a peak and then decreasing with increasing inclusion size. Numerical simulations of macro-structural responses (vibration, tension, impact and wave dispersion) demonstrate that the proposed model accurately captures the dynamic behavior of heterogeneous materials and structures. Compared to classical elastodynamic model, the strain gradient elastodynamics model mitigates stress singularities and reduces mesh sensitivity. In addition, compared to higher-order truncated elastodynamic model, the present model can achieve an optimal balance between accuracy and computational cost.

CRediT authorship contribution statement

Quanzhang Li: Writing – original draft, Visualization, Methodology, Formal analysis, Conceptualization. **Yipeng Rao:** Writing – review & editing, Validation. **Zihao Yang:** Writing – review & editing, Validation. **Junzhi Cui:** Writing – review & editing, Validation, Supervision, Conceptualization. **Meizhen Xiang:** Writing – review & editing, Validation, Supervision, Methodology, Conceptualization.

Declaration of competing interest

The authors declare that they have no known competing financial interests or personal relationships that could have appeared to influence the work reported in this paper.

Acknowledgments

This work is supported by National Natural Science Foundation of China (No. 12272061).

Appendix A. Centrosymmetric microstructure

We show that, for centrosymmetric microstructure, the odd-order tensors \mathbf{G}, \mathbf{H} vanish. Firstly, we prove the anti-centrosymmetry of the first order cell functions:

$$\mathbf{N}^{pq}(y_1, y_2, y_3) = -\mathbf{N}^{pq}(1 - y_1, 1 - y_2, 1 - y_3), \forall p, q \in \{1, 2, 3\}. \quad (\text{A.1})$$

By multiplying Eq. (9) by the test function $\mathbf{v} \in D(Y)$ and integrating over the normalized unit cell Y , the variational form is obtained:

$$\int_Y a_{ijpq} e_{yij}(\mathbf{v}) + a_{ijmn} e_{ymn}(\mathbf{N}^{pq}) e_{yij}(\mathbf{v}) d\mathbf{y} = 0, \forall p, q \in \{1, 2, 3\}. \quad (\text{A.2})$$

Define the vector-valued function $\bar{\mathbf{N}}^{11}(\mathbf{y}) = -\mathbf{N}^{11}(1 - y_1, 1 - y_2, 1 - y_3)$ and the corresponding test function $\bar{\mathbf{v}}(\mathbf{y}) = -\mathbf{v}(1 - y_1, 1 - y_2, 1 - y_3)$. By substituting $\bar{\mathbf{N}}^{11}(\mathbf{y}), \bar{\mathbf{v}}(\mathbf{y})$ into Eq. (A.2), we can obtain

$$\int_{Y_\epsilon} a_{ijpq} e_{yij}(\bar{\mathbf{v}}) + a_{ijmn} e_{ymn}(\bar{\mathbf{N}}^{pq}) e_{yij}(\bar{\mathbf{v}}) d\mathbf{y} = 0, \forall p, q \in \{1, 2, 3\}. \quad (\text{A.3})$$

It can be observed that for all $p, q \in \{1, 2, 3\}$, $\mathbf{N}^{pq}(\mathbf{y})$ and $\bar{\mathbf{N}}^{pq}(\mathbf{y})$ satisfy the same variational formulation. Therefore, we conclude that $\mathbf{N}^{pq}(\mathbf{y}) = \bar{\mathbf{N}}^{pq}(\mathbf{y})$. This anti-centrosymmetry result, along with the definitions of \mathbf{G} and \mathbf{H} (as outlined in Eqs. (21) and (25)), further leads to the conclusion that

$$G_{ijklm} = H_{ijk} = 0, \quad \forall i, j, k, l, m \in \{1, 2, 3\}. \quad (\text{A.4})$$

Appendix B. Numbers of independent components of $\mathbf{C}, \mathbf{D}, \mathbf{F}$

In this section, we investigate the independent components of $\mathbf{C}, \mathbf{D}, \mathbf{F}$ for inclusions of two different symmetry classes.

We begin by examining inclusions with orthotropic symmetry, such as ellipsoidal inclusions. Specifically, for the normalized unit cell $Y = [0, 1] \times [0, 1] \times [0, 1]$, the symmetry properties of the corresponding material parameters are described as:

$$\begin{aligned} a_{ijkl}(y_1, y_2, y_3) &= a_{ijkl}(1 - y_1, y_2, y_3) = a_{ijkl}(y_1, 1 - y_2, y_3) = a_{ijkl}(y_1, y_2, 1 - y_3), \\ \rho(y_1, y_2, y_3) &= \rho(1 - y_1, y_2, y_3) = \rho(y_1, 1 - y_2, y_3) = \rho(y_1, y_2, 1 - y_3). \end{aligned} \quad (\text{B.1})$$

Using a method analogous to the proof in Appendix A, we can establish the symmetry and anti-symmetry properties of all cell functions $\mathbf{N}^{pq}(y_1, y_2, y_3), \forall p, q \in \{1, 2, 3\}$ as:

$$\begin{cases} \text{When } p = q : \\ \mathbf{N}_i^{pq}(y_1, y_2, y_3) = (-1)^{\delta_{i1}} \mathbf{N}_i^{pq}(1 - y_1, y_2, y_3) = (-1)^{\delta_{i2}} \mathbf{N}_i^{pq}(y_1, 1 - y_2, y_3) = (-1)^{\delta_{i3}} \mathbf{N}_i^{pq}(y_1, y_2, 1 - y_3), \forall i \in \{1, 2, 3\}; \\ \text{When } p \neq q : \\ \mathbf{N}_i^{pq}(y_1, y_2, y_3) = (-1)^{\delta_{q1}} \mathbf{N}_i^{pq}(1 - y_1, y_2, y_3) = (-1)^{\delta_{q2}} \mathbf{N}_i^{pq}(y_1, 1 - y_2, y_3) = (-1)^{\delta_{q3}} \mathbf{N}_i^{pq}(y_1, y_2, 1 - y_3), i = p; \\ \mathbf{N}_i^{pq}(y_1, y_2, y_3) = (-1)^{\delta_{p1}} \mathbf{N}_i^{pq}(1 - y_1, y_2, y_3) = (-1)^{\delta_{p2}} \mathbf{N}_i^{pq}(y_1, 1 - y_2, y_3) = (-1)^{\delta_{p3}} \mathbf{N}_i^{pq}(y_1, y_2, 1 - y_3), i = q; \\ \mathbf{N}_i^{pq}(y_1, y_2, y_3) = -\mathbf{N}_i^{pq}(1 - y_1, y_2, y_3) = -\mathbf{N}_i^{pq}(y_1, 1 - y_2, y_3) = -\mathbf{N}_i^{pq}(y_1, y_2, 1 - y_3), i \neq p, i \neq q. \end{cases} \quad (\text{B.2})$$

Based on the symmetry and anti-symmetry properties of the first-order cell functions and the integral-form definitions of \mathbf{C}, \mathbf{D} , and \mathbf{F} (as outlined in Eqs. (20), (22), and (26)), we can deduce that the number of independent components for \mathbf{C}, \mathbf{D} , and \mathbf{F} is reduced to 9, 51, and 9, respectively. The corresponding Voigt matrix representations are shown in Fig. B.1.

Next, we consider inclusions with cubic symmetry, such as spherical and cubic inclusions. Building on the symmetry properties outlined in Eq. (B.1), the material parameters exhibit an even higher degree of symmetry, expressed as follows:

$$a_{ijkl}(y_1, y_2, y_3) = a_{ijkl}(y_{\tau(1)}, y_{\tau(2)}, y_{\tau(3)}), \rho(y_1, y_2, y_3) = \rho(y_{\tau(1)}, y_{\tau(2)}, y_{\tau(3)}). \quad (\text{B.3})$$

Here, τ represents a permutation of the indices 1, 2, 3.

Using similar computations, we can deduce additional symmetry and anti-symmetry properties of \mathbf{N}^{pq} as:

$$\mathbf{N}_k^{ij}(y_1, y_2, y_3) = \mathbf{N}_{\tau(k)}^{\tau(i)\tau(j)}(y_{\tau(1)}, y_{\tau(2)}, y_{\tau(3)}). \quad (\text{B.4})$$

Consequently, the number of independent components for $\mathbf{C}, \mathbf{D}, \mathbf{F}$ is further reduced to 3, 11, 3 respectively, as shown in Fig. B.2.

Appendix C. Eigenvalues variations of $\mathbf{C}, \mathbf{D}, \mathbf{F}$

In this section, we present the trends of all the eigenvalues of $\mathbf{C}, \mathbf{D}, \mathbf{F}$ with respect to the inclusion size. For spherical inclusions, Fig. C.1 supplements the information provided in Fig. 6. For cubic inclusions, Fig. C.2 complements the results shown in Fig. 9.

$$\begin{pmatrix}
C_{1111} & C_{1122} & C_{1133} & 0 & 0 & 0 \\
& C_{2222} & C_{2233} & 0 & 0 & 0 \\
& & C_{3333} & 0 & 0 & 0 \\
& & & C_{1212} & 0 & 0 \\
& & & & C_{1313} & 0 \\
& & & & & C_{2323}
\end{pmatrix}
\begin{pmatrix}
F_{1111} & F_{1122} & F_{1133} & 0 & 0 & 0 \\
& F_{2222} & F_{2233} & 0 & 0 & 0 \\
& & F_{3333} & 0 & 0 & 0 \\
& & & & F_{1212} & 0 \\
& & & & & F_{1313} \\
& & & & & & F_{2323}
\end{pmatrix}$$

$$\left(\begin{array}{ccccccccc}
D_{111111} & D_{111221} & D_{111331} & D_{111122} & D_{111133} & 0 & 0 & 0 & 0 & 0 & 0 & 0 & 0 & 0 & 0 & 0 \\
D_{221221} & D_{221331} & D_{221122} & D_{221133} & 0 & 0 & 0 & 0 & 0 & 0 & 0 & 0 & 0 & 0 & 0 & 0 \\
D_{331331} & D_{331122} & D_{331133} & 0 & 0 & 0 & 0 & 0 & 0 & 0 & 0 & 0 & 0 & 0 & 0 & 0 \\
D_{122122} & D_{122133} & 0 & 0 & 0 & 0 & 0 & 0 & 0 & 0 & 0 & 0 & 0 & 0 & 0 & 0 \\
D_{133133} & 0 & 0 & 0 & 0 & 0 & 0 & 0 & 0 & 0 & 0 & 0 & 0 & 0 & 0 & 0 \\
D_{131131} & D_{131232} & D_{131113} & D_{131223} & D_{131333} & 0 & 0 & 0 & 0 & 0 & 0 & 0 & 0 & 0 & 0 & 0 \\
D_{232232} & D_{232113} & D_{232223} & D_{232333} & 0 & 0 & 0 & 0 & 0 & 0 & 0 & 0 & 0 & 0 & 0 & 0 \\
D_{113113} & D_{113223} & D_{113333} & 0 & 0 & 0 & 0 & 0 & 0 & 0 & 0 & 0 & 0 & 0 & 0 & 0 \\
D_{223223} & D_{223333} & 0 & 0 & 0 & 0 & 0 & 0 & 0 & 0 & 0 & 0 & 0 & 0 & 0 & 0 \\
D_{333333} & 0 & 0 & 0 & 0 & 0 & 0 & 0 & 0 & 0 & 0 & 0 & 0 & 0 & 0 & 0 \\
D_{121121} & D_{121112} & D_{121222} & D_{121332} & D_{121233} & 0 & 0 & 0 & 0 & 0 & 0 & 0 & 0 & 0 & 0 & 0 \\
D_{112112} & D_{112222} & D_{112332} & D_{112233} & 0 & 0 & 0 & 0 & 0 & 0 & 0 & 0 & 0 & 0 & 0 & 0 \\
D_{222222} & D_{222332} & D_{222233} & 0 & 0 & 0 & 0 & 0 & 0 & 0 & 0 & 0 & 0 & 0 & 0 & 0 \\
D_{332332} & D_{332233} & 0 & 0 & 0 & 0 & 0 & 0 & 0 & 0 & 0 & 0 & 0 & 0 & 0 & 0 \\
D_{233233} & 0 & 0 & 0 & 0 & 0 & 0 & 0 & 0 & 0 & 0 & 0 & 0 & 0 & 0 & 0 \\
D_{231231} & D_{231132} & D_{231123} & 0 & 0 & 0 & 0 & 0 & 0 & 0 & 0 & 0 & 0 & 0 & 0 & 0 \\
D_{132132} & D_{132123} & D_{123123} & 0 & 0 & 0 & 0 & 0 & 0 & 0 & 0 & 0 & 0 & 0 & 0 & 0
\end{array} \right)$$

Fig. B.1. The structure of $\mathbf{C}, \mathbf{D}, \mathbf{F}$ for inclusions with orthotropic symmetry.

Appendix D. Some proofs

In this appendix, we provide the rigorous proofs for the conclusions presented in the main text. First, we present a lemma which establishes the linear independence of the first-order cell functions \mathbf{N}^{pq} .

Lemma 1. If there exist $0 < \alpha_0 < \beta_0$, $0 < \rho_0 < \rho_1$ such that $\forall \mathbf{m} \in \text{sym}(\mathcal{R}^{3 \times 3})$, $\mathbf{y} \in Y$:

$$\alpha_0 |\mathbf{m}|_F^2 \leq a_{ijkl}(\mathbf{y}) m_{ij} m_{kl}, \quad |\mathbf{A}(\mathbf{y}) : \mathbf{m}|_F \leq \beta_0 |\mathbf{m}|_F \quad (\text{D.1a})$$

$$\rho(\mathbf{y}) \geq \rho_0, \quad \rho(\mathbf{y}) \leq \rho_1, \quad (\text{D.1b})$$

then $\forall \mathbf{m} \neq 0 \in \text{sym}(\mathcal{R}^{3 \times 3})$,

$$\sum_{p,q} m_{pq} \mathbf{N}^{pq} \neq 0 \text{ in the sense of } D(Y). \quad (\text{D.2})$$

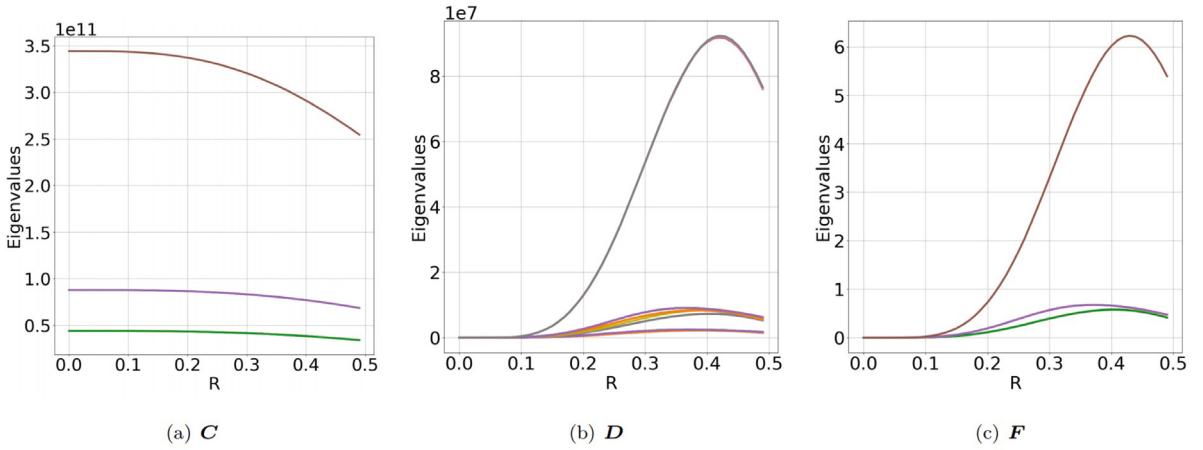
Based on the aforementioned lemma, we prove the symmetric positive definiteness of \mathbf{C} , \mathbf{D} , and \mathbf{F} in the main text. Here, we establish the existence and uniqueness of the solution to Eq. (47) by leveraging the symmetric positive definiteness of \mathbf{C} , \mathbf{D} , \mathbf{F} , and employing the Faedo–Galerkin method (see [80]).

Proof. STEP 1: Let $\{\mathbf{w}_l\}$ be the orthonormal basis in $(L^2(\Omega))^3$, Denote by V_N the N -dimensional subspace of $(H_0^2(\Omega))^3$ spanned by $\mathbf{w}_1, \dots, \mathbf{w}_N$. Additionally, we introduce the projection operator:

$$P_N(\mathbf{v}) = \sum_{q=1}^N (\mathbf{v}, \mathbf{w}_q)_{L^2(\Omega)} \mathbf{w}_q, \quad \forall \mathbf{v} \in L^2(\Omega). \quad (\text{D.3})$$

$$\begin{pmatrix}
\textcolor{red}{C}_{1111} & \textcolor{blue}{C}_{1122} & \textcolor{blue}{C}_{1133} & 0 & 0 & 0 \\
\textcolor{red}{C}_{2222} & \textcolor{blue}{C}_{2233} & 0 & 0 & 0 \\
\textcolor{red}{C}_{3333} & 0 & 0 & 0 \\
& \textcolor{green}{C}_{1212} & 0 & 0 \\
& & \textcolor{green}{C}_{1313} & 0 \\
& & & \textcolor{green}{C}_{2323}
\end{pmatrix}
\begin{pmatrix}
\textcolor{red}{F}_{1111} & \textcolor{blue}{F}_{1122} & \textcolor{blue}{F}_{1133} & 0 & 0 & 0 \\
\textcolor{red}{F}_{2222} & \textcolor{blue}{F}_{2233} & 0 & 0 & 0 \\
\textcolor{red}{F}_{3333} & 0 & 0 & 0 \\
& \textcolor{green}{F}_{1212} & 0 & 0 \\
& & \textcolor{green}{F}_{1313} & 0 \\
& & & \textcolor{green}{F}_{2323}
\end{pmatrix}$$

$$\left(\begin{array}{cccccccccccccc}
\textcolor{red}{D}_{111111} & \textcolor{red}{D}_{111221} & \textcolor{red}{D}_{111331} & \textcolor{blue}{D}_{111122} & \textcolor{blue}{D}_{111133} & 0 & 0 & 0 & 0 & 0 & 0 & 0 & 0 & 0 & 0 & 0 & 0 \\
\textcolor{yellow}{D}_{221221} & \textcolor{blue}{D}_{221331} & \textcolor{blue}{D}_{221122} & \textcolor{red}{D}_{221133} & 0 & 0 & 0 & 0 & 0 & 0 & 0 & 0 & 0 & 0 & 0 & 0 & 0 \\
\textcolor{yellow}{D}_{331331} & \textcolor{red}{D}_{331122} & \textcolor{red}{D}_{331133} & 0 & 0 & 0 & 0 & 0 & 0 & 0 & 0 & 0 & 0 & 0 & 0 & 0 & 0 \\
\textcolor{blue}{D}_{122122} & \textcolor{orange}{D}_{122133} & 0 & 0 & 0 & 0 & 0 & 0 & 0 & 0 & 0 & 0 & 0 & 0 & 0 & 0 & 0 \\
\textcolor{blue}{D}_{133133} & 0 & 0 & 0 & 0 & 0 & 0 & 0 & 0 & 0 & 0 & 0 & 0 & 0 & 0 & 0 & 0 \\
\textcolor{blue}{D}_{131131} & \textcolor{orange}{D}_{131232} & \textcolor{red}{D}_{131113} & \textcolor{red}{D}_{131223} & \textcolor{blue}{D}_{131333} & 0 & 0 & 0 & 0 & 0 & 0 & 0 & 0 & 0 & 0 & 0 & 0 \\
\textcolor{blue}{D}_{232232} & \textcolor{red}{D}_{232113} & \textcolor{blue}{D}_{232223} & \textcolor{blue}{D}_{232333} & 0 & 0 & 0 & 0 & 0 & 0 & 0 & 0 & 0 & 0 & 0 & 0 & 0 \\
\textcolor{yellow}{D}_{113113} & \textcolor{blue}{D}_{113223} & \textcolor{blue}{D}_{113333} & 0 & 0 & 0 & 0 & 0 & 0 & 0 & 0 & 0 & 0 & 0 & 0 & 0 & 0 \\
\textcolor{yellow}{D}_{223223} & \textcolor{blue}{D}_{223333} & 0 & 0 & 0 & 0 & 0 & 0 & 0 & 0 & 0 & 0 & 0 & 0 & 0 & 0 & 0 \\
\textcolor{red}{D}_{333333} & 0 & 0 & 0 & 0 & 0 & 0 & 0 & 0 & 0 & 0 & 0 & 0 & 0 & 0 & 0 & 0 \\
\textcolor{blue}{D}_{121121} & \textcolor{red}{D}_{121112} & \textcolor{blue}{D}_{121222} & \textcolor{red}{D}_{121332} & \textcolor{blue}{D}_{121233} & 0 & 0 & 0 & 0 & 0 & 0 & 0 & 0 & 0 & 0 & 0 & 0 \\
\textcolor{yellow}{D}_{112112} & \textcolor{blue}{D}_{112222} & \textcolor{blue}{D}_{112332} & \textcolor{blue}{D}_{112233} & 0 & 0 & 0 & 0 & 0 & 0 & 0 & 0 & 0 & 0 & 0 & 0 & 0 \\
\textcolor{red}{D}_{222222} & \textcolor{blue}{D}_{222332} & \textcolor{blue}{D}_{222233} & 0 & 0 & 0 & 0 & 0 & 0 & 0 & 0 & 0 & 0 & 0 & 0 & 0 & 0 \\
\textcolor{yellow}{D}_{332332} & \textcolor{blue}{D}_{332233} & 0 & 0 & 0 & 0 & 0 & 0 & 0 & 0 & 0 & 0 & 0 & 0 & 0 & 0 & 0 \\
\textcolor{blue}{D}_{233233} & 0 & 0 & 0 & 0 & 0 & 0 & 0 & 0 & 0 & 0 & 0 & 0 & 0 & 0 & 0 & 0 \\
\textcolor{blue}{D}_{231231} & \textcolor{red}{D}_{231132} & \textcolor{blue}{D}_{231123} & 0 & 0 & 0 & 0 & 0 & 0 & 0 & 0 & 0 & 0 & 0 & 0 & 0 & 0 \\
\textcolor{blue}{D}_{132132} & \textcolor{red}{D}_{132123} & \textcolor{blue}{D}_{132123} & 0 & 0 & 0 & 0 & 0 & 0 & 0 & 0 & 0 & 0 & 0 & 0 & 0 & 0 \\
\textcolor{blue}{D}_{123123} & 0 & 0 & 0 & 0 & 0 & 0 & 0 & 0 & 0 & 0 & 0 & 0 & 0 & 0 & 0 & 0
\end{array} \right)$$

Fig. B.2. The structure of $\mathbf{C}, \mathbf{D}, \mathbf{F}$ for inclusions with cubic symmetry.**Fig. C.1.** Variation of all eigenvalues of CDF with normalized radius R for a spherical inclusion.

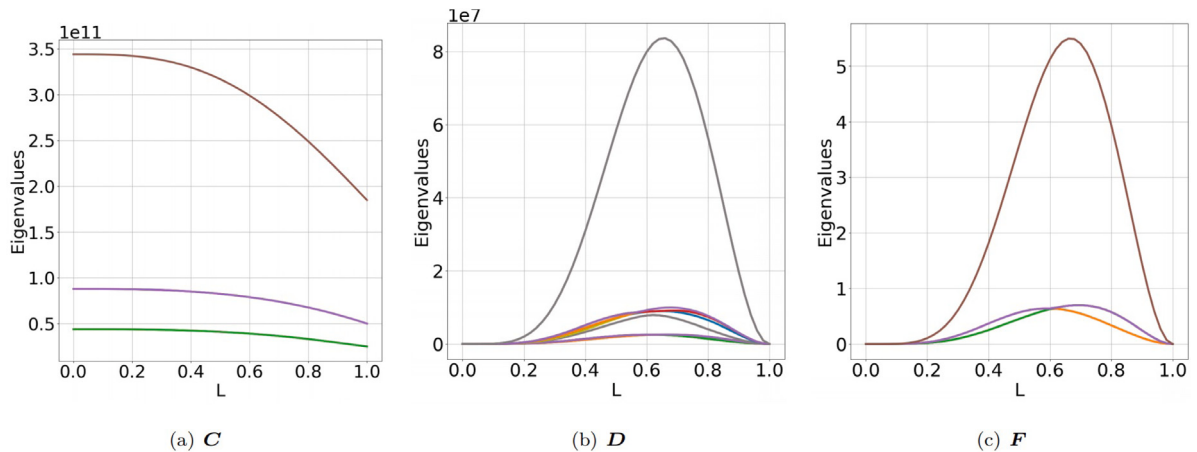


Fig. C.2. Variation of all eigenvalues of CDF with normalized side length L for a cubic inclusion.

Introduce, for any $N \in \mathbb{N}$ the finite dimensional approximate problem:

$$\left\{ \begin{array}{l} \text{find } \mathbf{u}_N = \sum_{p=1}^N g_p^N(t) \mathbf{w}_p \in V_N, \text{ such that :} \\ \int_{\Omega} \hat{\rho} \ddot{\mathbf{u}}_N \mathbf{w}_q d\mathbf{x} + \int_{\Omega} \varepsilon^2 F_{ijkl} e_{ij}(\ddot{\mathbf{u}}_N) e_{kl}(\mathbf{w}_q) d\mathbf{x} + a(\mathbf{u}_N, \mathbf{w}_q) = \int_{\Omega} \mathbf{f} \mathbf{w}_q d\mathbf{x}, \text{ in } (0, T) \times \Omega, \forall q = 1, 2, \dots, N, \quad (\text{a}) \\ \mathbf{u}^N(0) = \mathbf{u}_0^N = P_N(\mathbf{u}_0), \text{ in } \Omega, \quad (\text{b}) \\ \dot{\mathbf{u}}^N(0) = \mathbf{u}_1^N = P_N(\mathbf{u}_1), \text{ in } \Omega. \quad (\text{c}) \end{array} \right.$$

From (D.4b) and (D.4c), we have:

$$\mathbf{u}_0^N \rightarrow \mathbf{u}^0 \text{ in } (H_0^2(\Omega))^3, \quad (\text{D.5})$$

$$\mathbf{u}_1^N \rightarrow \mathbf{u}^1 \text{ in } (H_0^1(\Omega))^3. \quad (\text{D.6})$$

This problem is equivalent to the following system of N second-order linear ordinary differential equations with unknowns g_1^N, \dots, g_N^N :

$$\begin{cases} \hat{\rho}\ddot{g}_q^N(t) + \epsilon^2 \dot{g}_p^N(t) F_{ijkl} \int_{\Omega} e_{ij}(\mathbf{w}_p) e_{kl}(\mathbf{w}_q) d\mathbf{x} + g_p^N(t) a(\mathbf{w}_p, \mathbf{w}_q) = \int_{\Omega} \mathbf{f} \mathbf{w}_q d\mathbf{x}, \forall q = 1, 2, \dots, N, \\ g_p^N(0) = (\mathbf{u}_0, \mathbf{w}_p)_{L^2(\Omega)}, \forall p = 1, 2, \dots, N, \\ g_p^N(0) = (\mathbf{u}_1, \mathbf{w}_p)_{L^2(\Omega)}, \forall p = 1, 2, \dots, N. \end{cases} \quad (D.7)$$

Let us define:

$$A_{pq} = \rho \delta_{pq} + \varepsilon^2 \int_{\Omega} e_{ij}(\mathbf{w}_p) F_{ijkl} e_{kl}(\mathbf{w}_q) d\mathbf{x}, \quad B_{pq} = a(\mathbf{w}_p, \mathbf{w}_q).$$

From Eq. (40b) and the non-negativity of $\hat{\rho}$, we conclude that \mathbf{A} is a symmetric positive definite matrix, which implies that \mathbf{A} is invertible. Then Eq. (D.7a) can be rewritten as:

$$A\ddot{g}^N + Bg^N = \tilde{f} \Leftrightarrow \frac{d}{dt} \begin{pmatrix} \dot{g}^N \\ g^N \end{pmatrix} = \begin{pmatrix} A^{-1}(\tilde{f} - Bg^N) \\ \dot{g}^N \end{pmatrix} \Leftrightarrow \frac{d\tilde{g}^N}{dt} = \tilde{f}(t, \tilde{g}^N). \quad (D.8)$$

where

$$\bar{f}_q = \int_O \mathbf{f} \mathbf{w}_q d\mathbf{x}, \quad \tilde{\mathbf{g}}^N = \begin{pmatrix} \hat{\mathbf{g}}^N \\ \mathbf{g}^N \end{pmatrix}. \quad (\text{D.9})$$

According to the Picard-Lindelöf theorem, if the function $\tilde{f}(t, \tilde{\mathbf{g}}^N)$ satisfies the Lipschitz condition with respect to $\tilde{\mathbf{g}}^N$ and is continuous in the variables $\{t, \tilde{\mathbf{g}}^N\}$, then there exists a unique solution to the initial value problem on a certain time interval $(0, T)$. In particular, if \mathbf{f} is continuous with respect to t , this condition is clearly satisfied, thereby establishing the existence of the solution. Additionally, we have $g_p(t) \in C^1(0, T)$, indicating that each $g_p(t)$ is continuously differentiable on the interval $(0, T)$.

STEP 2: We will now prove that \mathbf{u}^N , satisfies some a priori estimates. To do so, let us multiply both side of Eq. (D.4a) by \dot{g}_q^N , and sum over q . This yields:

$$\left\{ \int_{\Omega} \hat{\rho} \dot{\mathbf{u}}^N \dot{\mathbf{u}}^N dx + \int_{\Omega} \varepsilon^2 e_{ij}(\dot{\mathbf{u}}^N) F_{ijkl} e_{kl}(\dot{\mathbf{u}}^N) dx + a(\mathbf{u}^N, \dot{\mathbf{u}}^N) \right\} = \int_{\Omega} \mathbf{f} \dot{\mathbf{u}}^N dx, \quad (\text{D.10})$$

which is equivalent to the following, based on the symmetry of \mathbf{F} :

$$\begin{aligned} \frac{d}{dt} \left\{ \int_{\Omega} \hat{\rho} \dot{\mathbf{u}}^N \dot{\mathbf{u}}^N dx + \int_{\Omega} \varepsilon^2 e_{ij}(\dot{\mathbf{u}}^N) F_{ijkl} e_{kl}(\dot{\mathbf{u}}^N) dx + a(\mathbf{u}^N, \dot{\mathbf{u}}^N) \right\} &= 2 \|\mathbf{f}\|_{L^2(\Omega)} \|\dot{\mathbf{u}}^N\|_{L^2(\Omega)} \\ &\leq \|\mathbf{f}\|_{L^2(\Omega)}^2 + \|\dot{\mathbf{u}}^N\|_{L^2(\Omega)}^2. \end{aligned} \quad (\text{D.11})$$

Integrating on $(0, t)$ with $t \leq T$, and using the ellipticity of $\mathbf{C}, \mathbf{D}, \mathbf{F}$ we obtain:

$$\begin{aligned} &\int_{\Omega} \hat{\rho} \dot{\mathbf{u}}^N(t) \dot{\mathbf{u}}^N(t) dx + \int_{\Omega} \varepsilon^2 e_{ij}(\dot{\mathbf{u}}^N)(t) F_{ijkl} e_{kl}(\dot{\mathbf{u}}^N)(t) dx + a(\mathbf{u}^N(t), \dot{\mathbf{u}}^N(t)) \\ &\leq \int_{\Omega} \hat{\rho} \dot{\mathbf{u}}^N(0) \dot{\mathbf{u}}^N(0) dx + \int_{\Omega} \varepsilon^2 e_{ij}(\dot{\mathbf{u}}^N)(0) F_{ijkl} e_{kl}(\dot{\mathbf{u}}^N)(0) dx + a(\mathbf{u}^N(0), \mathbf{u}^N(0)) + \int_0^T \|\mathbf{f}(\tau)\|_{L^2(\Omega)}^2 d\tau + \int_0^t \|\dot{\mathbf{u}}^N(\tau)\|_{L^2(\Omega)}^2 d\tau \\ &\leq c_1 \|\mathbf{u}_1^N\|_{H^1(\Omega)}^2 + \varepsilon^2 c_2 \|\mathbf{u}_0^N\|_{H^2(\Omega)}^2 + \int_0^T \|\mathbf{f}(\tau)\|_{L^2(\Omega)}^2 d\tau + \int_0^t \|\dot{\mathbf{u}}^N(\tau)\|_{L^2(\Omega)}^2 d\tau. \end{aligned} \quad (\text{D.12})$$

On the other hand, based on the second Korn inequality and the positive definiteness of $\mathbf{C}, \mathbf{D}, \mathbf{F}$, there exists a constant $c_3 > 0$ such that:

$$\begin{aligned} &\left\{ \int_{\Omega} \hat{\rho} \dot{\mathbf{u}}^N(t) \dot{\mathbf{u}}^N(t) dx + \int_{\Omega} \varepsilon^2 e_{ij}(\dot{\mathbf{u}}^N)(t) F_{ijkl} e_{kl}(\dot{\mathbf{u}}^N)(t) dx + a(\mathbf{u}^N(t), \dot{\mathbf{u}}^N(t)) \right\} \\ &\geq c_3 (\|\dot{\mathbf{u}}^N(t)\|_{H^1(\Omega)}^2 + \|\mathbf{u}^N(t)\|_{H_0^2(\Omega)}^2). \end{aligned} \quad (\text{D.13})$$

Therefore, we have

$$\|\dot{\mathbf{u}}^N(t)\|_{H^1(\Omega)}^2 + \|\mathbf{u}^N(t)\|_{H_0^2(\Omega)}^2 \leq c_4 (\|\mathbf{u}_1^N\|_{H^1(\Omega)}^2 + \|\mathbf{u}_0^N\|_{H_0^2(\Omega)}^2 + \|\mathbf{f}\|_{L^2((0,T) \times \Omega)}^2) + c_5 \int_0^t \|\dot{\mathbf{u}}^N(\tau)\|_{L^2(\Omega)}^2 d\tau. \quad (\text{D.14})$$

Applying the Gronwall inequality, we deduce the a priori estimate:

$$\|\dot{\mathbf{u}}^N(t)\|_{L^\infty(0,T; H^1(\Omega))} + \|\mathbf{u}^N(t)\|_{L^\infty(0,T; H_0^2(\Omega))} \leq c_6 (\|\mathbf{u}_1^N\|_{H^1(\Omega)}^2 + \|\mathbf{u}_0^N\|_{H_0^2(\Omega)}^2 + \|\mathbf{f}\|_{L^2((0,T) \times \Omega)}^2). \quad (\text{D.15})$$

It remains to obtain an a priori estimate for $\ddot{\mathbf{u}}^N$. Observe that Eq. (D.4a) implies that:

$$(\ddot{\mathbf{u}}_i^N(t), v_i)_{L^2(\Omega)} + (-\varepsilon^2 \partial_j(F_{ijkl} e_{kl}(\dot{\mathbf{u}}^N)), v_i)_{L^2(\Omega)} = (-\partial_j C_{ijkl} e_{kl}(\mathbf{u}^N) + \varepsilon^2 \partial_{jk} D_{ijklmn} e_{lmn}(\mathbf{u}^N) + f_i, v_i), \forall v \in V_N. \quad (\text{D.16})$$

This signifies that:

$$\ddot{\mathbf{u}}_i^N(t) - \varepsilon^2 \partial_j(F_{ijkl} e_{kl}(\dot{\mathbf{u}}^N)) = \partial_j C_{ijkl} e_{kl}(\mathbf{u}^N) - \varepsilon^2 \partial_{jk} D_{ijklmn} e_{lmn}(\mathbf{u}^N) + f_i, \text{ in } H^{-2}(\Omega). \quad (\text{D.17})$$

Then we have:

$$\begin{aligned} \|\ddot{\mathbf{u}}_i^N(t) - \varepsilon^2 \partial_j(F_{ijkl} e_{kl}(\dot{\mathbf{u}}^N))\|_{H^{-2}(\Omega)} &\leq \|\partial_j C_{ijkl} e_{kl}(\mathbf{u}^N)\|_{H^{-2}(\Omega)} + \|-\varepsilon^2 \partial_{jk} D_{ijklmn} e_{lmn}(\mathbf{u}^N)\|_{H^{-2}(\Omega)} + \|\mathbf{f}\|_{H^{-2}(\Omega)} \\ &\leq c_7 \|e_{kl}(\mathbf{u}^N)\|_{H_0^1(\Omega)} + \varepsilon^2 c_8 \|e_{lmn}(\mathbf{u}^N)\|_{L^2(\Omega)} + \|\mathbf{f}\|_{L^2(\Omega)} \\ &\leq c_9 (\|\mathbf{u}^N\|_{H_0^2(\Omega)} + \|\mathbf{f}\|_{L^2(\Omega)}). \end{aligned} \quad (\text{D.18})$$

Therefore

$$\begin{aligned} \|\ddot{\mathbf{u}}_i^N(t) - \varepsilon^2 \partial_j(F_{ijkl} e_{kl}(\dot{\mathbf{u}}^N))\|_{L^2(0,T; H^{-2}(\Omega))} &+ \|\dot{\mathbf{u}}^N(t)\|_{L^\infty(0,T; H^1(\Omega))} + \|\mathbf{u}^N(t)\|_{L^\infty(0,T; H_0^2(\Omega))} \\ &\leq c (\|\mathbf{u}_1^N\|_{H^1(\Omega)}^2 + \|\mathbf{u}_0^N\|_{H_0^2(\Omega)}^2 + \|\mathbf{f}\|_{L^2((0,T) \times \Omega)}^2), \end{aligned} \quad (\text{D.19})$$

where c depends only on $\{\alpha_2, \alpha_3, \alpha_3, \beta_2, \beta_3, \beta_3, \varepsilon, \Omega, T\}$.

STEP 3: In this step we pass to the limit in the approximate problem. Estimate Eq. (D.19) implies, up to a subsequence the following convergences:

$$\begin{cases} \mathbf{u}^N \rightharpoonup \mathbf{u} \text{ weakly* in } L^\infty(0, T; H_0^2(\Omega)), \\ \dot{\mathbf{u}}^N \rightharpoonup \dot{\mathbf{u}} \text{ weakly* in } L^\infty(0, T; H^1(\Omega)), \\ \ddot{\mathbf{u}}_i^N(t) - \varepsilon^2 \partial_j(F_{ijkl} e_{kl}(\dot{\mathbf{u}}^N)) \rightharpoonup \ddot{\mathbf{u}}_i(t) - \varepsilon^2 \partial_j(F_{ijkl} e_{kl}(\dot{\mathbf{u}}^N)) \text{ weakly in } L^2(0, T; H^{-2}(\Omega)). \end{cases} \quad (\text{D.20})$$

Let $\psi(t) \in C_0^\infty(0, T)$, $\mathbf{v} \in (H_0^2(\Omega))^3$. Multiplying both sides of Eq. (D.4a) by $(\mathbf{v}, \mathbf{w}_q)_{L^2(\Omega)} \psi$, summing over q , and integrating over $(0, T)$, we obtain:

$$\begin{aligned} &\int_0^T \int_{\Omega} \hat{\rho} \dot{\mathbf{u}}^N(\mathbf{x}, t) \psi(t) P_N(\mathbf{v})(\mathbf{x}) + \varepsilon^2 F_{ijkl} e_{ij}(\dot{\mathbf{u}}^N(\mathbf{x}, t)) \psi(t) e_{kl}(P_N(\mathbf{v}))(\mathbf{x}) dx dt + \int_0^T a(\mathbf{u}^N(t), \psi(t) P_N(\mathbf{v})) dt \\ &= \int_0^T \int_{\Omega} \mathbf{f}(\mathbf{x}, t) \psi(t) P_N(\mathbf{v})(\mathbf{x}) dx dt. \end{aligned}$$

By integration by parts with respect to t , one has:

$$\begin{aligned} & - \int_0^T \int_{\Omega} \hat{\rho} \dot{\mathbf{u}}^N(\mathbf{x}, t) \psi(t) P_N(\mathbf{v})(\mathbf{x}) + \varepsilon^2 F_{ijkl} e_{ij}(\dot{\mathbf{u}}^N(\mathbf{x}, t)) \psi(t) e_{kl}(P_N(\mathbf{v}))(\mathbf{x}) d\mathbf{x} dt + \int_0^T a(u^N(t), \psi(t) P_N(\mathbf{v})) dt \\ & = \int_0^T \int_{\Omega} \mathbf{f}(\mathbf{x}, t) \psi(t) P_N(\mathbf{v})(\mathbf{x}) d\mathbf{x} dt. \end{aligned}$$

Let us now pass to the limit $N \rightarrow \infty$:

$$\begin{aligned} & - \int_0^T \int_{\Omega} \hat{\rho} \dot{\mathbf{u}}(\mathbf{x}, t) \psi(t) \mathbf{v}(\mathbf{x}) + \varepsilon^2 F_{ijkl} e_{ij}(\dot{\mathbf{u}}(\mathbf{x}, t)) \psi(t) e_{kl}(\mathbf{v})(\mathbf{x}) d\mathbf{x} dt + \int_0^T a(\mathbf{u}(t), \psi(t) \mathbf{v}) dt = \int_0^T \int_{\Omega} \mathbf{f}(\mathbf{x}, t) \psi(t) \mathbf{v}(\mathbf{x}) d\mathbf{x} dt \\ & \Rightarrow \int_0^T \int_{\Omega} \hat{\rho} \dot{\mathbf{u}}(\mathbf{x}, t) \psi(t) \mathbf{v}(\mathbf{x}) + \varepsilon^2 F_{ijkl} e_{ij}(\dot{\mathbf{u}}(\mathbf{x}, t)) \psi(t) e_{kl}(\mathbf{v})(\mathbf{x}) d\mathbf{x} dt + \int_0^T a(\mathbf{u}(t), \psi(t) \mathbf{v}) dt = \int_0^T \int_{\Omega} \mathbf{f}(\mathbf{x}, t) \psi(t) \mathbf{v}(\mathbf{x}) d\mathbf{x} dt. \end{aligned}$$

STEP 4: It remains to check that the initial conditions $\mathbf{u}(0) = \mathbf{u}_0, \dot{\mathbf{u}}(0) = \mathbf{u}_1$ are satisfied. Let $\psi(t) \in C^\infty(0, T)$ such that $\psi'(0) = 1, \psi'(T) = 0$, and $\mathbf{v} \in (H_0^2(\Omega))^3$. Multiplying both sides of Eq. (D.4a) by $(\mathbf{v}, \mathbf{w}_q)_{L^2(\Omega)} \psi$, sum over q , and integral $(0, T)$, we obtain:

$$\begin{aligned} & \int_0^T \int_{\Omega} \hat{\rho} \dot{\mathbf{u}}^N(\mathbf{x}, t) \psi(t) P_N(\mathbf{v})(\mathbf{x}) + \varepsilon^2 F_{ijkl} e_{ij}(\dot{\mathbf{u}}^N(\mathbf{x}, t)) \psi(t) e_{kl}(P_N(\mathbf{v}))(\mathbf{x}) d\mathbf{x} dt + \int_0^T a(\mathbf{u}^N(t), \psi(t) P_N(\mathbf{v})) dt \\ & = \int_0^T \int_{\Omega} \mathbf{f}(\mathbf{x}, t) \psi(t) P_N(\mathbf{v})(\mathbf{x}) d\mathbf{x} dt \\ & \Rightarrow - \int_0^T \int_{\Omega} \hat{\rho} \dot{\mathbf{u}}^N(\mathbf{x}, t) \psi(t) P_N(\mathbf{v})(\mathbf{x}) + \varepsilon^2 F_{ijkl} e_{ij}(\dot{\mathbf{u}}^N(\mathbf{x}, t)) \psi(t) e_{kl}(P_N(\mathbf{v}))(\mathbf{x}) d\mathbf{x} dt + \int_0^T a(\mathbf{u}^N(t), \psi(t) P_N(\mathbf{v})) dt \\ & = \int_0^T \int_{\Omega} \mathbf{f}(\mathbf{x}, t) \psi(t) P_N(\mathbf{v})(\mathbf{x}) d\mathbf{x} dt + \int_{\Omega} \hat{\rho} \mathbf{u}_1^N(\mathbf{x}) + \varepsilon^2 F_{ijkl} e_{ij}(\mathbf{u}_1^N(\mathbf{x})) e_{kl}(P_N(\mathbf{v}))(\mathbf{x}) d\mathbf{x} \\ & \Rightarrow - \int_0^T \int_{\Omega} \hat{\rho} \dot{\mathbf{u}}(\mathbf{x}, t) \psi(t) \mathbf{v}(\mathbf{x}) + \varepsilon^2 F_{ijkl} e_{ij}(\dot{\mathbf{u}}(\mathbf{x}, t)) \psi(t) e_{kl}(\mathbf{v})(\mathbf{x}) d\mathbf{x} dt + \int_0^T a(\mathbf{u}(t), \psi(t) \mathbf{v}) dt \\ & = \int_0^T \int_{\Omega} \mathbf{f}(\mathbf{x}, t) \psi(t) \mathbf{v}(\mathbf{x}) d\mathbf{x} dt + \int_{\Omega} \hat{\rho} \mathbf{u}_1(\mathbf{x}) \mathbf{v}(\mathbf{x}) + \varepsilon^2 F_{ijkl} e_{ij}(\mathbf{u}_1(\mathbf{x})) e_{kl}(\mathbf{v})(\mathbf{x}) d\mathbf{x} \\ & \Rightarrow \int_0^T (\hat{\rho} \dot{\mathbf{u}}_i(t) - \varepsilon^2 \partial_j [F_{ijkl} e_{kl}(\dot{\mathbf{u}})], \psi(t) \mathbf{v})_{H^{-2}(\Omega), H_0^2(\Omega)} dt + \int_0^T a(\mathbf{u}(t), \psi(t) \mathbf{v}) dt + \int_{\Omega} \hat{\rho} \dot{\mathbf{u}}_i(\mathbf{x}, 0) + \varepsilon^2 F_{ijkl} e_{kl}(\dot{\mathbf{u}})(\mathbf{x}, 0) e_{ij}(\mathbf{v})(\mathbf{x}) d\mathbf{x} \\ & = \int_0^T \int_{\Omega} \mathbf{f}(\mathbf{x}, t) \psi(t) \mathbf{v}(\mathbf{x}) d\mathbf{x} dt + \int_{\Omega} \hat{\rho} \mathbf{u}_1(\mathbf{x}) \mathbf{v}(\mathbf{x}) + \varepsilon^2 F_{ijkl} e_{ij}(\mathbf{u}_1(\mathbf{x})) e_{kl}(\mathbf{v})(\mathbf{x}) d\mathbf{x}. \end{aligned}$$

Therefore, we have

$$\begin{aligned} & \int_{\Omega} \hat{\rho} \mathbf{u}_1(\mathbf{x}) \mathbf{v}(\mathbf{x}) + \varepsilon^2 F_{ijkl} e_{ij}(\mathbf{u}_1(\mathbf{x})) e_{kl}(\mathbf{v})(\mathbf{x}) d\mathbf{x} = \int_{\Omega} \hat{\rho} \dot{\mathbf{u}}(\mathbf{x}, 0) + \varepsilon^2 F_{ijkl} e_{kl}(\dot{\mathbf{u}})(\mathbf{x}, 0) e_{ij}(\mathbf{v})(\mathbf{x}) d\mathbf{x}, \forall \mathbf{v} \in H_0^2(\Omega) \\ & \Leftrightarrow \int_{\Omega} \hat{\rho} \mathbf{u}_1(\mathbf{x}) \mathbf{v}(\mathbf{x}) - \varepsilon^2 \partial_j [F_{ijkl} e_{ij}(\mathbf{u}_1(\mathbf{x}))] \mathbf{v}(\mathbf{x}) d\mathbf{x} = \int_{\Omega} \hat{\rho} \dot{\mathbf{u}}_i(\mathbf{x}, 0) - \varepsilon^2 \partial_j [F_{ijkl} e_{kl}(\dot{\mathbf{u}})](\mathbf{x}, 0) \mathbf{v}(\mathbf{x}) d\mathbf{x}, \forall \mathbf{v} \in H_0^2(\Omega). \end{aligned}$$

After subtracting both sides of the equation, we obtain the following expression:

$$\int_{\Omega} \hat{\rho} (\mathbf{u}_1(\mathbf{x}) - \dot{\mathbf{u}}(\mathbf{x}, 0)) \mathbf{v}(\mathbf{x}) + \varepsilon^2 F_{ijkl} (e_{ij}(\mathbf{u}_1(\mathbf{x}) - \dot{\mathbf{u}}(\mathbf{x}, 0))) e_{kl}(\mathbf{v})(\mathbf{x}) d\mathbf{x} = 0, \forall \mathbf{v} \in C_0^\infty(\Omega) \quad (\text{D.21})$$

Subsequently, by choosing the test function as $\mathbf{v}(\mathbf{x}) = \mathbf{u}_1(\mathbf{x}) - \dot{\mathbf{u}}(\mathbf{x}, 0)$, it follows that:

$$\dot{\mathbf{u}}(\mathbf{x}, 0) = \mathbf{u}_1(\mathbf{x}). \quad (\text{D.22})$$

Analogously, we obtain

$$\mathbf{u}(\mathbf{x}, 0) = \mathbf{u}_0(\mathbf{x}). \quad (\text{D.23})$$

By employing the conventional technique of taking differences between solutions, the uniqueness of the solutions can be readily demonstrated. \square

Data availability

Data will be made available on request.

References

- [1] A. Carpinteri, Scaling laws and renormalization groups for strength and toughness of disordered materials, *Int. J. Solids Struct.* 31 (3) (1994) 291–302.
- [2] A. Carpinteri, Mechanical Damage and Crack Growth in Concrete: Plastic Collapse To Brittle Fracture, Vol. 5, Springer Science & Business Media, 2012.
- [3] D.C. Lam, F. Yang, A. Chong, J. Wang, P. Tong, Experiments and theory in strain gradient elasticity, *J. Mech. Phys. Solids* 51 (8) (2003) 1477–1508.
- [4] R. Peerlings, N. Fleck, Computational evaluation of strain gradient elasticity constants, *Int. J. Multiscale Comput. Eng.* 2 (4) (2004).
- [5] I. Goda, J.-F. Ganghoffer, Construction of first and second order grade anisotropic continuum media for 3d porous and textile composite structures, *Compos. Struct.* 141 (2016) 292–327.
- [6] S. Sahmani, M.M. Aghdam, T. Rabczuk, Nonlinear bending of functionally graded porous micro/nano-beams reinforced with graphene platelets based upon nonlocal strain gradient theory, *Compos. Struct.* 186 (2018) 68–78.
- [7] I. Goda, R. Rahouadj, J.-F. Ganghoffer, Size dependent static and dynamic behavior of trabecular bone based on micromechanical models of the trabecular architecture, *Internat. J. Engrg. Sci.* 72 (2013) 53–77.
- [8] I. Goda, M. Assidi, J.-F. Ganghoffer, A 3d elastic micropolar model of vertebral trabecular bone from lattice homogenization of the bone microstructure, *Biomech. Model. Mechanobiol.* 13 (2014) 53–83.
- [9] M. Haque, M. Saif, Strain gradient effect in nanoscale thin films, *Acta Mater.* 51 (11) (2003) 3053–3061.
- [10] B. Wang, S. Zhou, J. Zhao, X. Chen, A size-dependent kirchhoff micro-plate model based on strain gradient elasticity theory, *Eur. J. Mech. A Solids* 30 (4) (2011) 517–524.
- [11] J. Zhao, S. Zhou, B. Wang, X. Wang, Nonlinear microbeam model based on strain gradient theory, *Appl. Math. Model.* 36 (6) (2012) 2674–2686.
- [12] E.C. Aifantis, On the role of gradients in the localization of deformation and fracture, *Internat. J. Engrg. Sci.* 30 (10) (1992) 1279–1299.
- [13] S. Hosseini, J. Niiranen, 3D strain gradient elasticity: Variational formulations, isogeometric analysis and model peculiarities, *Comput. Methods Appl. Mech. Engrg.* 389 (2022) 114324.
- [14] A.C. Eringen, Linear theory of nonlocal elasticity and dispersion of plane waves, *Internat. J. Engrg. Sci.* 10 (5) (1972) 425–435.
- [15] A.C. Eringen, Theory of nonlocal thermoelasticity, *Internat. J. Engrg. Sci.* 12 (12) (1974) 1063–1077.
- [16] A.C. Eringen, J. Wegner, Nonlocal continuum field theories, *Appl. Mech. Rev.* 56 (2) (2003) B20–B22.
- [17] S.A. Silling, M. Epton, O. Weckner, J. Xu, E. Askari, Peridynamic states and constitutive modeling, *J. Elasticity* 88 (2007) 151–184.
- [18] S.A. Silling, R.B. Lehoucq, Peridynamic theory of solid mechanics, *Adv. Appl. Mech.* 44 (2010) 73–168.
- [19] F. Han, G. Lubineau, Y. Azdoud, Adaptive coupling between damage mechanics and peridynamics: A route for objective simulation of material degradation up to complete failure, *J. Mech. Phys. Solids* 94 (2016) 453–472.
- [20] E.M.P. Cosserat, F. Cosserat, Théorie des corps déformables, A. Hermann et fils, 1909.
- [21] R.D. Mindlin, H. Tiersten, et al., Effects of couple-stresses in linear elasticity, *Arch. Ration. Mech. Anal.* 11 (1) (1962) 415–448.
- [22] R.D. Mindlin, Micro-structure in linear elasticity, *Arch. Ration. Mech. Anal.* 16 (1964) 51–78.
- [23] R. Toupin, Elastic materials with couple-stresses, *Arch. Ration. Mech. Anal.* 11 (1) (1962) 385–414.
- [24] E.C. Aifantis, Update on a class of gradient theories, *Mech. Mater.* 35 (3–6) (2003) 259–280.
- [25] C. Lim, G. Zhang, J. Reddy, A higher-order nonlocal elasticity and strain gradient theory and its applications in wave propagation, *J. Mech. Phys. Solids* 78 (2015) 298–313.
- [26] A. Bacigalupo, L. Gambarotta, Second-gradient homogenized model for wave propagation in heterogeneous periodic media, *Int. J. Solids Struct.* 51 (5) (2014) 1052–1065.
- [27] G. Rosi, N. Auffray, Anisotropic and dispersive wave propagation within strain-gradient framework, *Wave Motion* 63 (2016) 120–134.
- [28] G. Ahmadi, K. Firoozbakhsh, First strain gradient theory of thermoelasticity, *Int. J. Solids Struct.* 11 (3) (1975) 339–345.
- [29] M. Shishesaz, M. Hosseini, K. Naderan Tahan, A. Hadi, Analysis of functionally graded nanodisks under thermoelastic loading based on the strain gradient theory, *Acta Mech.* 228 (2017) 4141–4168.
- [30] S. Khakalo, J. Niiranen, Anisotropic strain gradient thermoelasticity for cellular structures: Plate models, homogenization and isogeometric analysis, *J. Mech. Phys. Solids* 134 (2020) 103728.
- [31] N. Fleck, G. Müller, M.F. Ashby, J.W. Hutchinson, Strain gradient plasticity: theory and experiment, *Acta Met. et Mater.* 42 (2) (1994) 475–487.
- [32] M.E. Gurtin, On the plasticity of single crystals: free energy, microforces, plastic-strain gradients, *J. Mech. Phys. Solids* 48 (5) (2000) 989–1036.
- [33] C.-S. Han, H. Gao, Y. Huang, W.D. Nix, Mechanism-based strain gradient crystal plasticity theory, *J. Mech. Phys. Solids* 53 (5) (2005) 1188–1203.
- [34] H. Jiang, Y. Huang, Z. Zhuang, K. Hwang, Fracture in mechanism-based strain gradient plasticity, *J. Mech. Phys. Solids* 49 (5) (2001) 979–993.
- [35] J. Li, A micromechanics-based strain gradient damage model for fracture prediction of brittle materials—part I: Homogenization methodology and constitutive relations, *Int. J. Solids Struct.* 48 (24) (2011) 3336–3345.
- [36] J. Li, T. Pham, R. Abdelmoula, F. Song, C. Jiang, A micromechanics-based strain gradient damage model for fracture prediction of brittle materials—part II: Damage modeling and numerical simulations, *Int. J. Solids Struct.* 48 (24) (2011) 3346–3358.
- [37] L. Placidi, E. Barchiesi, A. Misra, A strain gradient variational approach to damage: a comparison with damage gradient models and numerical results, *Math. Mech. Complex Syst.* 6 (2) (2018) 77–100.
- [38] R. Sunyk, P. Steinmann, On higher gradients in continuum-atomistic modelling, *Int. J. Solids Struct.* 40 (24) (2003) 6877–6896.
- [39] M. Xiang, J. Cui, B. Li, X. Tian, Atom-continuum coupled model for thermo-mechanical behavior of materials in micro-nano scales, *Sci. China Phys. Mech. Astron.* 55 (2012) 1125–1137.
- [40] N.C. Admal, J. Marian, G. Po, The atomistic representation of first strain-gradient elastic tensors, *J. Mech. Phys. Solids* 99 (2017) 93–115.
- [41] W.J. Drugan, J.R. Willis, A micromechanics-based nonlocal constitutive equation and estimates of representative volume element size for elastic composites, *J. Mech. Phys. Solids* 44 (4) (1996) 497–524.
- [42] W. Drugan, Micromechanics-based variational estimates for a higher-order nonlocal constitutive equation and optimal choice of effective moduli for elastic composites, *J. Mech. Phys. Solids* 48 (6–7) (2000) 1359–1387.
- [43] M.G. Geers, V. Kouznetsova, W. Brekelmans, Gradient-enhanced computational homogenization for the micro-macro scale transition, *Le J. de Phys. IV* 11 (PR5) (2001) Pr5–145.
- [44] V. Kouznetsova, M.G. Geers, W.M. Brekelmans, Multi-scale constitutive modelling of heterogeneous materials with a gradient-enhanced computational homogenization scheme, *Internat. J. Numer. Methods Engrg.* 54 (8) (2002) 1235–1260.
- [45] J. Yvonnet, N. Auffray, V. Monchiet, Computational second-order homogenization of materials with effective anisotropic strain-gradient behavior, *Int. J. Solids Struct.* 191 (2020) 434–448.
- [46] A. Bensoussan, J.-L. Lions, G. Papanicolaou, T. Caughey, Asymptotic analysis of periodic structures, *J. Appl. Mech.* 46 (2) (1979) 477.
- [47] O. Oleinik, A. Shamaev, G. Yosifian, Mathematical Problems in Elasticity and Homogenization, Elsevier, 1992.
- [48] K. Terada, N. Kikuchi, A class of general algorithms for multi-scale analyses of heterogeneous media, *Comput. Methods Appl. Mech. Engrg.* 190 (40–41) (2001) 5427–5464.
- [49] N. Triantafyllidis, S. Bardenhagen, The influence of scale size on the stability of periodic solids and the role of associated higher order gradient continuum models, *J. Mech. Phys. Solids* 44 (11) (1996) 1891–1928.
- [50] V.P. Smyshlyayev, K.D. Cherednichenko, On rigorous derivation of strain gradient effects in the overall behaviour of periodic heterogeneous media, *J. Mech. Phys. Solids* 48 (6–7) (2000) 1325–1357.

- [51] S. Barboura, J. Li, Establishment of strain gradient constitutive relations by using asymptotic analysis and the finite element method for complex periodic microstructures, *Int. J. Solids Struct.* 136 (2018) 60–76.
- [52] W. Chen, J. Fish, A dispersive model for wave propagation in periodic heterogeneous media based on homogenization with multiple spatial and temporal scales, *J. Appl. Mech.* 68 (2) (2001) 153–161.
- [53] A. Bacigalupo, L. Gambarotta, Computational two-scale homogenization of periodic masonry: characteristic lengths and dispersive waves, *Comput. Methods Appl. Mech. Engrg.* 213 (2012) 16–28.
- [54] H. Yang, Z. Liu, Y. Xia, W. Fan, A.C. Taylor, X. Han, Mechanical properties of hierarchical lattice via strain gradient homogenization approach, *Compos. Part B: Eng.* 271 (2024) 111153.
- [55] Y. Rao, M. Xiang, J. Cui, A strain gradient brittle fracture model based on two-scale asymptotic analysis, *J. Mech. Phys. Solids* 159 (2022) 104752.
- [56] Y. Rao, M. Xiang, Q. Li, J. Cui, A unified two-scale theory for modeling microstructural length scale, strain gradient and strain rate effects on brittle fracture, *Int. J. Solids Struct.* 268 (2023) 112176.
- [57] A. Love, *A treatise on the mathematical theory of elasticity*, 1892.
- [58] S. Cowin, M. Mehrabadi, The structure of the linear anisotropic elastic symmetries, *J. Mech. Phys. Solids* 40 (7) (1992) 1459–1471.
- [59] N. Auffray, H. Le Quang, Q.-C. He, Matrix representations for 3d strain-gradient elasticity, *J. Mech. Phys. Solids* 61 (5) (2013) 1202–1223.
- [60] N. Auffray, Q.-C. He, H. Le Quang, Complete symmetry classification and compact matrix representations for 3d strain gradient elasticity, *Int. J. Solids Struct.* 159 (2019) 197–210.
- [61] S.-A. Papanicolopoulos, Chirality in isotropic linear gradient elasticity, *Int. J. Solids Struct.* 48 (5) (2011) 745–752.
- [62] N. Auffray, J. Dirrenberger, G. Rosi, A complete description of bi-dimensional anisotropic strain-gradient elasticity, *Int. J. Solids Struct.* 69 (2015) 195–206.
- [63] J. Niiranen, S. Khakalo, V. Balobanov, A.H. Niemi, Variational formulation and isogeometric analysis for fourth-order boundary value problems of gradient-elastic bar and plane strain/stress problems, *Comput. Methods Appl. Mech. Engrg.* 308 (2016) 182–211.
- [64] V.A. Eremeyev, S.A. Lurie, Y.O. Solyaev, F. dell'Isola, On the well posedness of static boundary value problem within the linear dilatational strain gradient elasticity, *Z. Für Angew. Math. Und Phys.* 71 (2020) 1–16.
- [65] N. Bakhalov, G. Panasenko, Homogenisation: Averaging processes in periodic media, *Math. Appl.* (1989).
- [66] D. Cioranescu, P. Donato, *An Introduction To Homogenization*, Oxford University Press, 1999.
- [67] H. Yang, B.E. Abali, D. Timofeev, W.H. Müller, Determination of metamaterial parameters by means of a homogenization approach based on asymptotic analysis, *Contin. Mech. Thermodyn.* 32 (2020) 1251–1270.
- [68] H. Yang, B.E. Abali, W.H. Müller, S. Barboura, J. Li, Verification of asymptotic homogenization method developed for periodic architected materials in strain gradient continuum, *Int. J. Solids Struct.* 238 (2022) 111386.
- [69] O. Keita, C. Dascalu, B. François, A two-scale model for dynamic damage evolution, *J. Mech. Phys. Solids* 64 (2014) 170–183.
- [70] S. Altan, E. Aifantis, On the structure of the mode iii crack-tip in gradient elasticity, *Scr. Met. et Mater.* 26 (2) (1992) 319–324.
- [71] C. Ru, E. Aifantis, A simple approach to solve boundary-value problems in gradient elasticity, *Acta Mech.* 101 (1) (1993) 59–68.
- [72] A.V. Metrikine, H. Askes, One-dimensional dynamically consistent gradient elasticity models derived from a discrete microstructure: Part 1: Generic formulation, *Eur. J. Mech. A Solids* 21 (4) (2002) 555–572.
- [73] H. Askes, A.V. Metrikine, One-dimensional dynamically consistent gradient elasticity models derived from a discrete microstructure: Part 2: Static and dynamic response, *Eur. J. Mech. A Solids* 21 (4) (2002) 573–588.
- [74] I.M. Gitman, H. Askes, E.C. Aifantis, The representative volume size in static and dynamic micro-macro transitions, *Int. J. Fract.* 135 (2005) L3–L9.
- [75] N.M. Newmark, A method of computation for structural dynamics, *J. Eng. Mech. Div.* 85 (3) (1959) 67–94.
- [76] J.N. Reddy, *An Introduction To the Finite Element Method*, Vol. 27, New York, 1993, p. 14.
- [77] H. Askes, E.C. Aifantis, Gradient elasticity in statics and dynamics: an overview of formulations, length scale identification procedures, finite element implementations and new results, *Int. J. Solids Struct.* 48 (13) (2011) 1962–1990.
- [78] D. Gross, C. Zhang, Wave propagation in damaged solids, *Int. J. Solids Struct.* 29 (14–15) (1992) 1763–1779.
- [79] A. Berezovski, M.E. Yildizdag, D. Scerrato, On the wave dispersion in microstructured solids, *Contin. Mech. Thermodyn.* 32 (2020) 569–588.
- [80] J.L. Lions, E. Magenes, *Non-Homogeneous Boundary Value Problems and Applications*, Vol. 1, Springer Science & Business Media, 2012, p. 181.